MODIFICATION OF SOLAR DRIVEN TIO$_2$ PHOTOCATALYST VIA DOPED AND CO DOPED METHODS FOR DEGRADATION OF METHYLENE BLUE

‘AIZAT AZHARI BIN MOHD YATIM

INSTITUTE OF GRADUATE STUDIES
UNIVERSITY OF MALAYA
KUALA LUMPUR

2017

MODIFICATION OF SOLAR DRIVEN TiO_2 PHOTOCATALYST VIA DOPED AND CO DOPED METHODS FOR DEGRADATION OF METHYLENE BLUE

‘AIZAT AZHARI BIN MOHD YATIM

**DISSERTATION SUBMITTED IN FULFILMENT OF
THE REQUIREMENTS FOR THE DEGREE OF MASTER
OF PHILOSOPHY**

**INSTITUTE OF GRADUATE STUDIES
UNIVERSITY OF MALAYA
KUALA LUMPUR**

2017

UNIVERSITY OF MALAYA

ORIGINAL LITERARY WORK DECLARATION

Name of Candidate: ‘AIZAT AZHARI BIN MOHD YATIM

(I.C/Passport No:

Matric No: HGA140024

Name of Degree: MASTER OF PHILOSOPHY

Title of Dissertation: MODIFICATION OF SOLAR DRIVEN TIO_2 PHOTOCATALYST VIA DOPED AND CO DOPED METHODS FOR DEGRADATION OF METHYLENE BLUE

Field of Study: CHEMISTRY

I do solemnly and sincerely declare that:

(1) I am the sole author/writer of this Work;
(2) This Work is original;
(3) Any use of any work in which copyright exists was done by way of fair dealing and for permitted purposes and any excerpt or extract from, or reference to or reproduction of any copyright work has been disclosed expressly and sufficiently and the title of the Work and its authorship have been acknowledged in this Work;
(4) I do not have any actual knowledge nor do I ought reasonably to know that the making of this work constitutes an infringement of any copyright work;
(5) I hereby assign all and every rights in the copyright to this Work to the University of Malaya (“UM”), who henceforth shall be owner of the copyright in this Work and that any reproduction or use in any form or by any means whatsoever is prohibited without the written consent of UM having been first had and obtained;
(6) I am fully aware that if in the course of making this Work I have infringed any copyright whether intentionally or otherwise, I may be subject to legal action or any other action as may be determined by UM.

Candidate’s Signature Date:

Witness’s Signature Date:

Name:

Designation

MODIFICATION OF SOLAR DRIVEN TiO_2 PHOTOCATALYST VIA DOPED AND CO DOPED METHODS FOR DEGRADATION OF METHYLENE BLUE

ABSTRACT

The presence of vanadium (V) and nitrogen (N) in titanium dioxide (TiO_2) nanoparticles enhanced its photocatalytic activity against degradation methylene blue (MB). Vanadium nitrogen co-doped TiO_2 (VN co-doped TiO_2) photocatalyst is synthesised by the modified sol–gel method. The corresponding samples for V doped TiO_2 (0.006 %, 0.125 %, 0.250 %, 0.500 %, 1.000 %) were labelled as V1 doped TiO_2, V2 doped TiO_2, V3 doped TiO_2, V4 doped TiO_2, and V5 doped TiO_2 while for N doped TiO_2 (0.100 %, 0.250 %, 0.500 %, 0.750 %, 1.000 %) were labelled as N1 doped TiO_2, N2 doped TiO_2, N3 doped TiO_2, N4 doped TiO_2, and N5 doped TiO_2. The subsequent photocatalysts were characterised using X-ray Diffraction (XRD), Brunauer-Emmet-Teller (BET), Raman Spectroscopy, UV–Vis Diffuse Reflectance Spectroscopy (DRS), Field Emission Scanning Electron Microscope (FESEM), Energy Dispersive X-ray (EDX) and X-ray Photoelectron Spectroscopy (XPS). The VN co-doped TiO_2 photocatalyst reported a narrower band gap (2.65 eV) compared to a single-doped V doped TiO_2 (2.89 eV), N doped TiO_2 (2.87 eV), and undoped TiO_2 (3.18 eV). Moreover, VN co-doped TiO_2 photocatalyst also demonstrated superior photocatalytic activity for the degradation of MB compared to the undoped and single-doped TiO_2 with almost 99 % of MB degradation in 120 minutes. The incorporation of V and N in the TiO_2 lattice resulted in isolated energy levels near the valence and conduction bands, which considerably narrowed the band gap. Furthermore, the recombination between photogenerated charges was reduced due to the low concentrations of dopants, since these energy levels can also trap photoexcited holes and electrons. The synergistic effects between V and N in TiO_2 increased the photocatalytic activity of VN co-doped TiO_2 nanoparticles.

Keywords: Photocatalyst, photodegradation, band gap, sol gel, doped and co doped.

PENGUBAHSUAIAN FOTOPEMANGKIN TIO_2 YANG DIDORONG OLEH TENAGA SOLAR MELALUI KAEDAH DOP DAN DOP BERSAMA UNTUK PENGURAIAN METILENA BIRU

ABSTRAK

Kehadiran vanadium (V) dan nitrogen (N) dalam partikel nano titanium dioksida (TiO_2) meningkatkan kadar aktiviti fotopemangkinan terhadap penguraian metilena biru (MB). TiO_2 didopkan bersama vanadium dan nitrogen (VN bersama didopkan TiO_2) fotomangkin disintesis melalui kaedah sol-gel yang diubah suai. Sampel yang sepadan untuk V didopkan TiO_2 (0.006 %, 0.125 %, 0.250 %, 0.500 %, 1.000 %) telah dilabelkan sebagai V1 didopkan TiO_2, V2 didopkan TiO_2, V3 didopkan TiO_2, V4 didopkan TiO_2, dan V5 didopkan TiO_2 manakala bagi N didopkan TiO_2 (0.100 %, 0.250 %, 0.500 %, 0.750 %, 1.000 %) telah dilabelkan sebagai N1 didopkan TiO_2, N2 didopkan TiO_2, N3 didopkan TiO_2, N4 didopkan TiO_2 dan N5 didopkan TiO_2. Fotomangkin berikutnya telah dicirikan menggunakan sinar-X Pembelauan (XRD), Brunauer-Emmet-Teller (BET), Raman Spektroskopi, UV-Vis Meresap Pantulan Spektroskopi (DRS), Raman Spektroskopi, Medan Pelepasan Mikroskop Imbasan Elektron (FESEM), Tenaga serakan X-ray (EDX) dan sinar-X fotoelektron Spektroskopi (XPS). The TiO_2 fotomangkin didopkan bersama VN melaporkan jalur jurang yang sempit (2.65 eV) berbanding dengan V2 tunggal didopkan didopkan TiO_2 (2.89 eV), N4 didopkan TiO_2 (2.87 eV) dan TiO_2 sahaja (3.18 eV). Tambahan pula, TiO_2 didopkan bersama VN fotomangkin juga menunjukkan aktiviti fotopemangkinan yang komited untuk penguraian MB berbanding TiO_2 yang tidak didopkan dan didopkan secara tunggal dengan hampir 99 % daripada MB penguraian dalam masa 120 minit. Pemerbadanan V dan N dalam kekisi TiO_2 yang menyumbang kepada tahap tenaga terpencil berhampiran valens dan pengaliran jalur, yang jauh merapatkan jurang jalur. Tambahan pula, penggabungan semula antara cas yang dihasilkan dari foto telah berkurangan disebabkan oleh kepekatan yang rendah bahan dop, kerana ini tahap tenaga boleh juga perangkap fotoketerujaan lubang dan elektron. Kesan sinergi antara V dan N dalam TiO_2 peningkatan aktiviti photopemangkinan daripada partikel nano TiO_2 didopkan bersama VN.

Keywords: Fotopemangkin, fotopenguraian, jalur jurang, sol gel, dop dan dop bersama,

ACKNOWLEDGEMENTS

This thesis would not have possible without the efforts and support of people at the Nanotechnology and Catalysis Research Centre (NANOCAT) and my surrounding friends.

First of all, I would like to express my deepest gratitude to my supervisor Dr Samira Bagheri her source of guidance, assistance and concern throughout my research project. Her wide knowledge and valuable comments have provided a good basis for my project and thesis.

Besides that, I would like to express a special thanks to all staffs in NANOCAT, faculty of Physic and chemistry in University Malaya (UM), respectively for their continuous guidance and assistance during all the samples preparation and testing. Most importantly, I would like to greatly acknowledge my colleagues in UM and all my dearest friends in NANOCAT. I deeply appreciated their precious ideas and support throughout the entire study. Lastly, I would like to take this opportunity to express my deepest gratitude to my beloved parents and all family members through their encouragement and support me to continue studying.

This research was supported by a grant from University Malaya Research Grant (UMRG) and Postgraduate Research Fund (PG059-2015B) for the sources of funding through this study. I gratefully acknowledge UM for financial supporting that helping me in this study and MyMaster scholarship from Ministry of High Education (MoHE).

I am indebted to my late supervisor, Allahyarhamah Prof. Dr. Sharifah Bee Abd Hamid, for her love, guidance, concern, constant encouragement, kind and support throughout the development of this research project. May her soul rest in peace.

Al-Fatihah

TABLE OF CONTENTS

LIST OF FIGURESS

LIST OF TABLES

LIST OF SYMBOLS AND ABBREVIATIONS

TiO_2 : Titanium Dioxide

V-TiO_2 : Vanadium doped TiO_2

N-TiO_2 : Nitrogen doped TiO_2

VN-TiO_2 : Vanadium Nitrogen co-doped TiO_2

MCL : Maximum Contaminant Level

MB : Methylene Blue

MO : Methylene Orange

CNT : Carbon Nanotube

DFT : Density Functional Theory

JCPDS : Joint Committee on Powder Diffraction Standards

e^- : Electron

h^+ : Positive hole

$^{\cdot}OH$: Hydroxyl radical

$^{\cdot}O_2^-$: Superoxide anion radical

eV : Electronvolt

mPa : Milli Pascal

IEP : Isoelectric Point

λ : Wavelength

FESEM : Field Emission Scanning Electron Microscope

XRD : X-ray Diffraction

BET : Brunauer-Emmet-Teller

EDX : Energy Dispersive X-ray

DRS : UV-Vis Diffuse Reflectance Spectroscopy

XPS : X-ray Photoelectron Spectroscopy

wt. %	:	Weight percent
BE	:	Binding energy
CTAB	:	Cetyltrimethylammonium bromide
V_2O_5	:	Vanadium oxide
NH_4VO_3	:	Ammonium metavanadate
$N(CH_2CH_3)_3$	:	Triethylamine
TTIP	:	Titanium isopropoxide

LIST OF APPENDICES

CHAPTER 1: INTRODUCTION

1.1 Research background

Water resources are abundant and renewable, however only less than 1 % of available water resources are potable (Tarver, 2008), which include ground water, springs, aquifers, rivers, and hyporheic zones. All processed drinking water must adhere to the national drinking water regulations for maximum contaminant level (MCL) in terms of its physical, chemical, bacteriological, and radioactivity properties. Although the quality of drinking water is satisfactory in most developed countries (Rosborg *et al.*, 2006), 783 million people lack access to safe drinking water (Clark *et al.*, 1995). Moreover, the hectic global industrial growth, especially in textile, pharmaceuticals, and agriculture led to the presence of various types of recalcitrant contaminants in the water system (Harris & McCartor, 2011). It is therefore crucial that contaminated water is effectively treated prior to being disposed into the environment or delegated to consumers for daily use.

One of the major water pollutants are the residual dyes from different sources (e.g., textile industries, paper, and pulp industries, dye, pharmaceutical industries, tannery, and craft bleaching industries, etc.). As shown in Figure 1.1, the World Bank estimated that the textile industries in many countries are the source of ~ 17 – 20 % of global industrial water pollution.

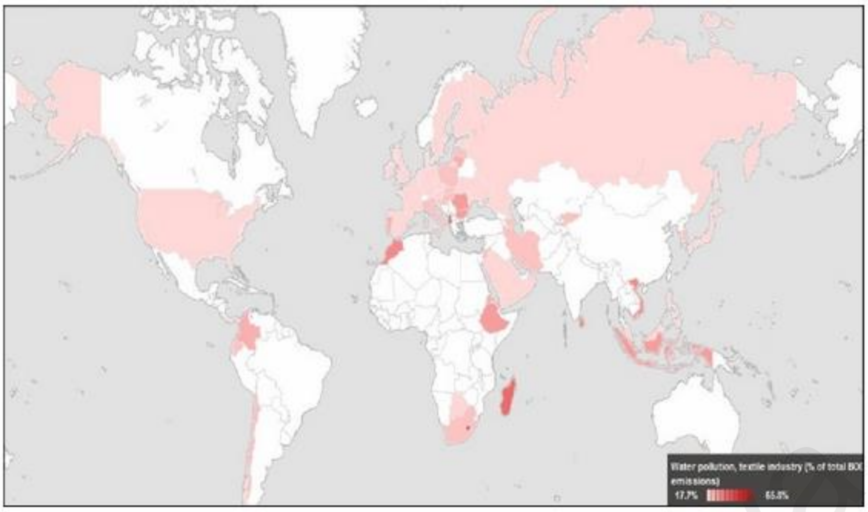

Figure 1.1: Water pollution caused by textile industrial from various countries. The darker icon signifies higher level of water pollution which is based on percentage of total biochemical oxygen demand (BOD) emissions (The World Bank, 2013)

1.1.1 Methylene blue (MB) as synthetic dye

Methylene blue (MB) is one of the most well-known organic dyes and water pollutant. It is therefore designated as the photocatalytic reactant in this work. Methylene blue (MB), is one of the basic dyes with a heterocyclic aromatic structure. The cationic dyes were frequently used in the initial step of dyeing silk, leather, plastics, printing inks, paper, and manufacturing paints (Berneth & Bayer, 2003). Its chemical formula is $C_{16}H_{18}N_3SCl$, while its structural formula is shown in Figure 1.2.

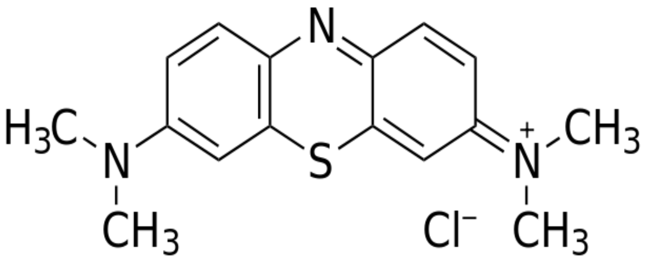

Figure 1.2: Structure of Methylene Blue (Yao *et al.*, 2010)

The discharge of the persistent toxic organic dyes might negatively affect health and the environment. Certain organic dyes form aromatic organic substances, which are carcinogenic and mutagenic, causing irritation in the eyes, skin, inflammation of respiratory tract, asthma, sore throat, and allergic contact dermatitis (Chequer *et al.*, 2013). These negative effects mainly apply to the non-biodegradable nature of the persistent organic dyes, as well as their high colour intensity and reduction of aquatic diversity by blocking the penetration of sunlight through water (Koswojo *et al.*, 2010). Furthermore, persistent organic dyes will remain in the environment for a long period of time in the event of incomplete treatments due to its inherent stability.

1.1.2 Relevant research on water treatment technology

There are numerous technologies that were developed to treat dye-contaminated water, such as liquid/solid phase adsorption, filtration, reverse osmosis, microbial degradation, electro-dialysis, chemical degradation, ion exchange, and coagulation and flocculating agent (Allegre *et al.*, 2006; Dąbrowski, 2001; Geetha & Velmani, 2015; McMullan *et al.*, 2001). Most conventional methods required high power and a skilful operator, which makes it economically unfeasible. In chemical treatment, disposal problems are caused by the accumulation of concentrated sludge. Moreover, the increased usage of excessive chemicals will result in secondary problems that are not immediately apparent.

Among the various methods, photocatalytic degradation using TiO_2 is most effective in treating a variety of refractory organic pollutants (Schneider *et al.*, 2014). The photocatalytic degradation of dye using TiO_2 has been studied since 1990 (Ahmed *et al.*, 2010; Akpan & Hameed, 2009; Chakrabarti & Dutta, 2004; Collazzo *et al.*, 2012; Lai *et al.*, 2014; Neppolian *et al.*, 2002).

1.1.3 Photocatalytic treatment using titanium dioxide nanoparticles

Titanium dioxide (TiO_2) nanoparticles are widely investigated semiconductor due to its versatility, low cost, stability, and environmental friendly. Previous works discussed the application of TiO_2 as photocatalyst, photovoltaics, water splitting devices, sensors, and CO_2 reduction for fuel generation (H. Park *et al.*, 2013). TiO_2 is one of the favoured semiconductors for photocatalytic and water purification due to its strategic redox position relative to other semiconductors such as Fe_2O_3, SnO_2, and WO_3 (Castellote & Bengtsson, 2011). There are various methods to synthesise TiO_2, such as the sol-gel, hydrothermal, solvothermal, chemical vapour deposition (CVD), and microwave methods (Akpan & Hameed, 2010; Balasubramanian *et al.*, 2004; Grätzel, 2001; Su *et al.*, 2004; Wang *et al.*, 2011). The sol-gel via alkoxide route is much more advantageous relative to other methods, due to its homogeneity, purity, and flexibility in introducing dopants at the molecular level to TiO_2 (Pookmanee & Phanichphant, 2009).

1.2 Problem statement

The photocatalytic activity of conventional TiO_2 in degrading pollutant is defined due to its wide band gap and inefficient electron/hole separation (Shon *et al.*, 2008). As a result of this, many studies dealt with improving TiO_2 properties. Efforts includes metal doping (Ag, Al, Cu, Co, Ni, Cr, Mn, Nb, V, Fe, Zn, Au, Pt, etc.), non-metal doping (N, C, S, F, P, etc.), dye sensitisation, heterogeneous composites (Al_2O_3, WO_3, CdS, etc.), hybridisation with nanomaterials (CNTs, fullerenes, graphene, zeolites, etc.) and dye-sensitisation and surface adsorbates (phosphates, surfactants, polymers, etc.) (Bach *et al.*, 1998; Chen & Mao, 2007; Gupta & Tripathi, 2011; Park *et al.*, 2013; Tan *et al.*, 2011; Zaleska, 2008). Recent attempt includes creating surface disorders by hydrogenation while preserving the crystallite core in TiO_2 (Liu *et al.*, 2005). This resulted in increased photocatalytic activity from the utilisation of 4 % of UV light and 45 % of visible light as light source. However, the remaining portion of the solar light (infra-red) remained unused. The photocatalytic activity of TiO_2 is commensurate to the amount of light absorbed (Chen *et al.*, 2012). Thus, it is important to design a TiO_2 that can absorb a wider range of solar light while efficiently separating electrons and holes.

It is also necessary to design a solar-drive photocatalyst that is capable of enhanced photodegradation activity and are less dependent on additional chemicals (Fenton reagent, oxidants, etc.). There is a need to circumvent the limitations associated with TiO_2 and its corresponding photocatalytic activity towards MB degradation.

1.3 Research scope

In order to enhance the photocatalytic activity under solar light irradiation, TiO_2 nanoparticles are synthesised and modified via the sol-gel method, cationic, and anionic doping, and the co-doping techniques. This study is divided into three stages.

Stage I involves the preparation of the photocatalyst via the sol-gel method in the presence of non-ionic surfactant to synthesise TiO_2 nanoparticles. Then, the TiO_2 nanoparticles were modified by doping with a cationic dopant, vanadium, and an anionic dopant, nitrogen, to improve solar light absorption and delay the electron/hole recombination. The selected molar ratio of dopants was subjected to the co-doping technique to enhance photocatalytic activity.

Four types of photocatalyst were prepared:

1) Undoped TiO_2 (without any dopant)
2) Vanadium doped TiO_2
3) Nitrogen doped TiO_2
4) Vanadium Nitrogen co-doped TiO_2

Stage II involves determining the physico-chemical properties of the photocatalysts by using X-Ray Diffraction (XRD), Brunner-Emmet-Teller (BET), UV-Vis diffuse reflectance spectroscopy (DRS), Raman spectroscopy, Field Emission Scanning Electron Microscope (FESEM), Electron Diffractive X-Ray (EDX), X-Ray Photoelectron Spectroscopy (XPS).

Stage III involves evaluating the photocatalytic activities of the prepared photocatalysts for the photodegradation of MB pollutant under solar light irradiation. The degradation products were subsequently analysed using the UV-Vis spectrophotometer.

1.4 Objectives

The objectives of this study are:

1. To synthesise the TiO_2 photocatalyst doped V and N at different composition via sol gel technique.
2. To characterise the photocatalyst in term of photoexcitation range and inhibition of electron/hole recombination.
3. To investigate the photocatalytic activity of photocatalyst for degradation of methylene blue under solar irradiation.

1.5 Organisation of Dissertation

This dissertation is structured into five chapters.

Chapter 1 - Present a general review of the current environmental issue related to water pollution and wastewater treatment. The limitation of the wastewater treatment on MB has been clearly described along with the objectives and scopes of the work.

Chapter 2 - Highlight literature view and research background of wastewater treatment technology, the mechanism of photocatalysis, TiO_2 photocatalysis, and the modification and photocatalytic activity of the photocatalyst towards degrading organic pollutants (MB).

Chapter 3 - Describe the synthesis of TiO_2 nanoparticles and its characterisation, followed by the modification of TiO_2 using doping / co-doping technique and the application of these photocatalysts for MB degradation.

Chapter 4 - Present and discuss the characterisation of synthesised undoped TiO_2 nanoparticles single doped TiO_2 nanoparticles, and co-doped TiO_2 nanoparticles and photocatalytic activities of all synthesised photocatalyst towards the degradation of MB.

Chapter 5 - Summarise the overall conclusions and discuss recommendations for future research proposal.

CHAPTER 2: LITERATURE REVIEW

2.1 Photocatalyst and photocatalysis

The pioneering work of Fujishima and Honda (1972) revealed the possibility of water splitting using a simple electrochemical cell supported-TiO_2 semiconductor setup. Researchers began taking note of the application of metal oxides in the energy sector. Since then, intensive research on semiconductors such as TiO_2, ZnO, and even C_3N_4 are investigated for the application of H_2 and CH_4 generation, air and water purification, and solar cells (Irie *et al.*, 2006).

The word photocatalysis consists of two parts, “photo” and “catalysis”. Catalysis is a process where a material is used to modify the rate of a chemical reaction by reducing the activation energy. This material is known as a catalyst, and is not altered or consumed at the end of the reaction. Photocatalysis is a reaction similar to catalysis, but uses light for its catalyst activation. In photocatalysis, the catalyst is known as the photocatalyst, which is a material that acts as a catalyst by altering the rate of a chemical reaction when exposed to light (Fujishima *et al.*, 2000).

2.2 Band structure

The ability to photo-excite electrons in any crystalline semiconductor using an external source of energy is the key factor for any photo-based application. These electrons populate the energy band, which is a collection of individual energy levels of electrons surrounding each atom. In an isolated atom, electrons only have discrete energy levels. However, in a crystalline solid, these energy level are split into many divisions due to the atomic interactions, which creates a continuous band of allowed energy states, such as the valence and conduction bands (Figure 2.1). The valence band is made up of occupied molecular orbitals and has an energy level that is lower than the conduction band. The conduction band has higher energy levels, and is generally empty. The distance between the valence and conduction bands in a semiconductor is called the band gap, which is where the Fermi level is located (50 % probability of occupied states) (Van Zeghbroeck, 2011).

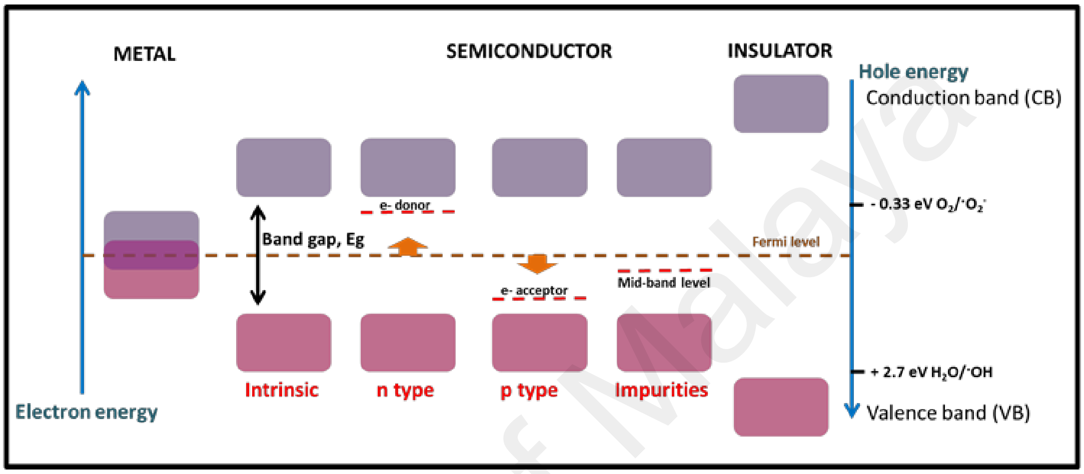

Figure 2.1: Valence and conduction band of metal, semiconductor and insulator (Djurisic *et al.*, 2014)

There are many types of semiconductors, with varying energy band position and band gap energies (Figure 2.2). In an intrinsic semiconductor, the Fermi level lies in the middle gap. The Fermi level for extrinsic semiconductors, such as the n-type and p-type, shifts towards the conduction band and valence band, respectively (Djurisic *et al.*, 2014; Van Zeghbroeck, 2011). In this context, metals and insulators cannot be used as a photocatalyst due to the less strategic position of the bands. In a metal, the electron flows freely due to the overlapping bands and the Fermi level already positioned in the conduction band. For insulators, the wide band gap (exceeding ~ 9 eV) requires a large amount of energy for photo-excitation (Brune *et al.*, 2008; Van Zeghbroeck, 2011).

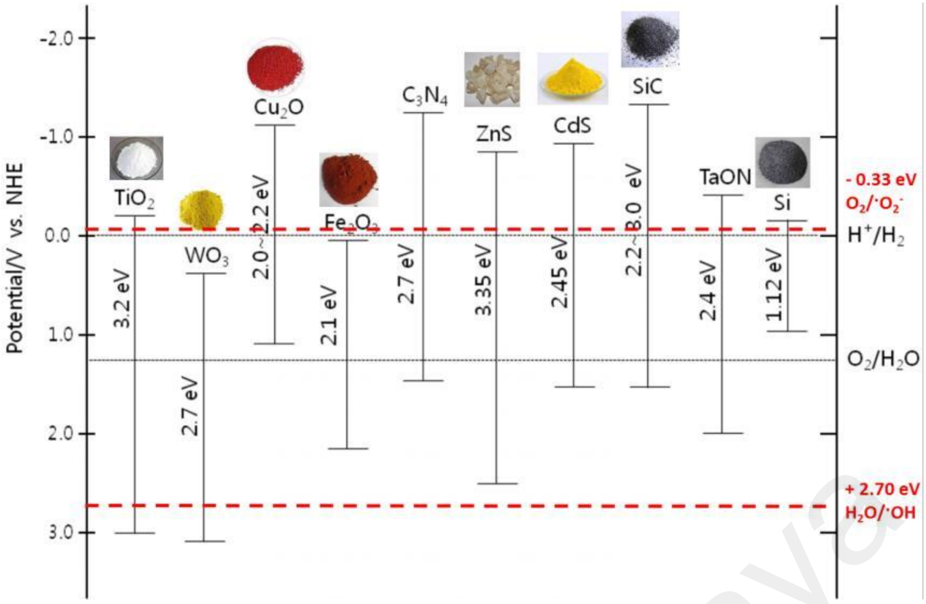

Figure 2.2: List of semiconductors and band gap positions (Chhowalla *et al.*, 2013)

2.3 Mechanism of photocatalyst

In a semiconductor photocatalyst, the absorption of energy that is equal to or greater than the band gap excites the electrons, e^-, in the valence band towards the conduction band, leaving a positive hole, h^+. The electrons and holes could also recombine on the bulk or the surface of the photocatalyst (Figure 2.3).

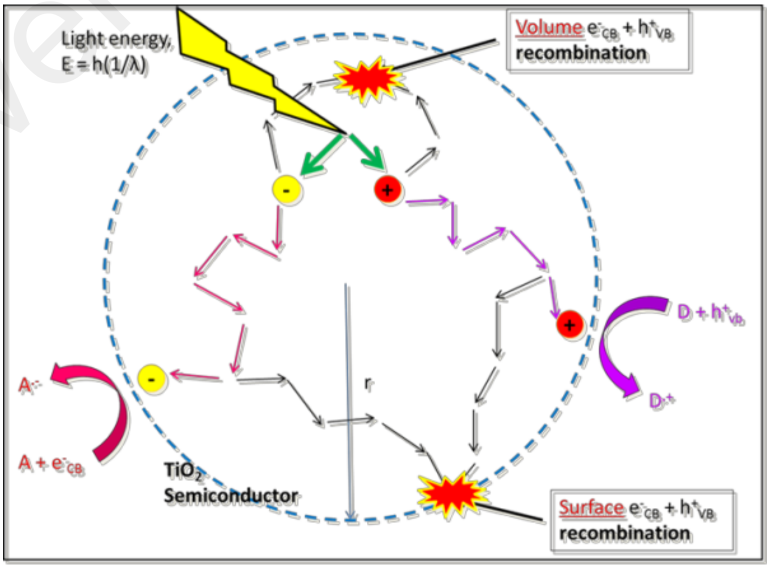

Figure 2.3: Bulk (volume) and surface electrons and holes recombination in a photocatalyst (Linsebigler *et al.*, 1995)

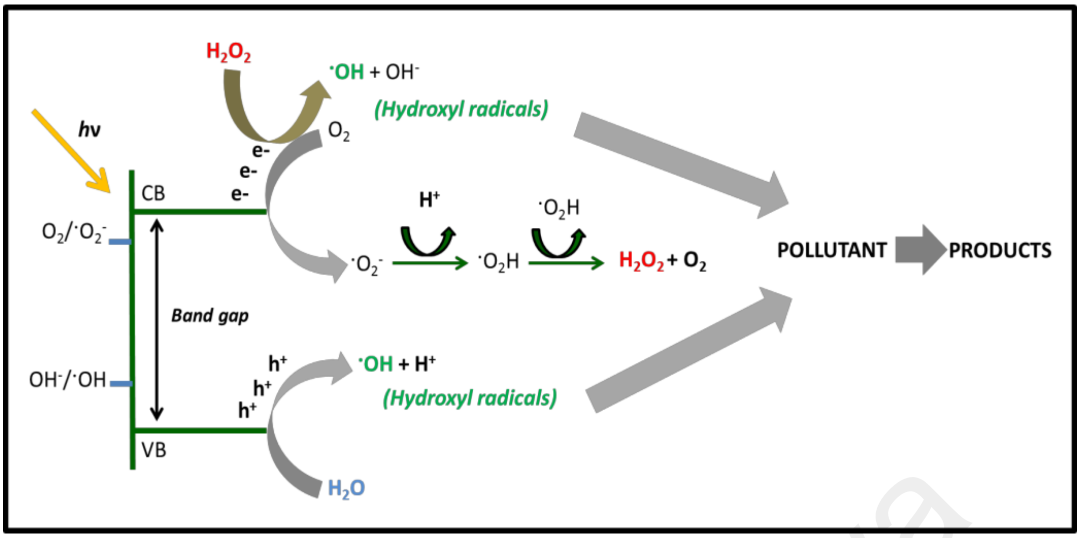

Figure 2.4: Photocatalytic degradation mechanisms of TiO_2 (Samsudin, Hamid, Juan, Basirun, & Centi, 2015)

Contrarily, the non-recombined charge carriers migrate to the catalyst surface and reacts with an electron acceptor (O_2) and donor (H_2O). In humid or aqueous environment, the positive holes (at the conduction band) react with absorbed water molecules or hydroxyl ions and forms hydroxyl radicals, $\cdot OH$. These radical in turn oxidises organic pollutants in a reaction called indirect oxidation. Direct oxidation occurs when the organic pollutant is oxidised directly by the conduction band holes. The photo-excited electrons at the valence band react with absorbed oxygen to form superoxide anion radicals, $\cdot O_2$-. These radicals, in turn, reduce the organic pollutant, and are regarded as an indirect reduction. Direct reduction occurs when the organic pollutant is reduced directly by the valence band electrons. In photocatalytic activity, $\cdot OH$ are mostly favoured due to its high oxidising potential relative to other radicals such as superoxide anion radicals, $\cdot O_2^-$ (Alfano *et al.*, 1997). The photocatalyst degradation mechanism is illustrated in Figure 2.4 and Table 2.1.

Table 2.1: Principle of a photocatalyst and radical formations

Path	Description	Mechanism
Photo-excitation of semiconductor		
(1)	Electron-hole pair generation	$Semiconductor + hv \rightarrow e_{CB}^- + h_{VB}^+$
(2)	Electron-hole pair recombination	$e_{CB}^- + h_{VB}^+ \rightarrow TiO_2 + heat$
Reaction at the conduction band		
(1)	An electron can migrate to the catalyst surface and directly reduces absorbed organic pollutant.	$D + e_{CB}^- \rightarrow {}^{\cdot}D^-$ Organic pollutant + e_{CB}^- → reduced species (direct)
(2)	An electron can migrate to the catalyst surface and reduce absorbed oxygen molecules and forms superoxide anion radicals.	$O_2 + e_{CB}^- \rightarrow {}^{\cdot}O^{2-}$ Organic pollutant + ·OH → reduced species (indirect)
(3)	Formation of hydroxyl radical from superoxide anion radicals via a reductive pathway.	$OO^{\cdot} + H^+ \rightarrow {}^{\cdot}OO$
(4)	Formation of hydrogen peroxide Formation of hydrogen peroxide and oxygen.	${}^{\cdot}OOH + H^+ \rightarrow H_20_2$ ${}^{\cdot}OOH + {}^{\cdot}OOH \rightarrow H_20_2 + O_2$
(5)	Formation of hydroxyl radical.	$H_2O_2 + e_{CB}^- \rightarrow OH^- + {}^{\cdot}OH$ Organic pollutant + ·OH → reduced species (indirect)
Reaction at the valence band		
(1)	A hole can migrate to the catalyst surface and directly oxidises absorbed organic pollutant.	$D + h_{VB}^+ \rightarrow D^+$ Organic pollutant + h_{VB}^+ → oxidised species (direct)
(2)	A hole can migrate to the catalyst surface and oxidise absorbed water molecules or surface hydroxyls and forms hydroxyl radicals.	$H_2O + h_{VB}^+ \rightarrow {}^{\cdot}OH^- + H^+$ Organic pollutant + ·OH → oxidised species (indirect)

(Linsebigler *et al.*, 1995)

2.4 Properties of titanium dioxide, TiO_2 semiconductor

Titanium dioxide, or TiO_2, belongs to the transition metal oxide group. It occurs in the form of three naturally occurring polymorphs, which are tetragonal anatase, rutile, and orthorhombic brookite (Castellote & Bengtsson, 2011; Diebold, 2003). Rutile is the most stable, whereby anatase and brookite could potentially transform into rutile due to their metastable properties (Gupta & Tripathi, 2011) . When titanium ions are paired with an oxide ligand to form TiO_2, there will be splitting of d-orbitals on titanium due to electron repulsion (Rozhkova & Ariga, 2015). The colour of intrinsic TiO_2 originated from the value of d-splitting energy of titanium ions when paired with oxide ligands, where all absorbed visible light is reflected, resulting in a white metal oxide. The properties of each TiO_2 polymorph are shown in Table 2.2.

Table 2.2: Properties and application of TiO_2

Properties	Anatase	Rutile	Brookite
Crystal structure	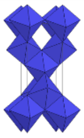 Tetragonal	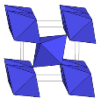 Tetragonal	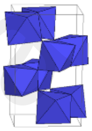 Orthorhombic
Lattice constant (Å)	$a = b = 3.784$ $c = 9.515$	$a = b = 4.5936$ $c = 2.9587$	$a = 9.184$ $b = 5.447$ $c = 5.154$
Density (g/cm^3)	3.79	4.13	3.99
Ti-O bond length (Å)	1.937 (4) 1.965 (2)	1.949 (4) 1.980 (2)	1.87 to 2.04
O-Ti-O bond angle	77.7° 92.6°	81.2° 90.0°	77.0° to 105°
Refractive index	2.56, 2.48	2.61, 2.90	2.58, 2.70
Band gap (eV)	3.05 to 3.23	2.98 to 3.02	3.1 to 3.4
Application	Photocatalyst, Pigments	Solar cells, Optics, Pigments, cosmetics	Difficult to prepare

(Castellote & Bengtsson, 2011; Gupta & Tripathi, 2011)

2.5 TiO_2 versus other materials as a photocatalyst

In TiO_2, the valence band is composed of O 2p orbitals hybridising with the Ti 3d orbitals, while the conduction band solely contains Ti 3d orbitals. The intrinsic position of the valence and conduction bands in TiO_2 is strategically located for the redox activity of most organic pollutants (Samsudin, Hamid, Juan, Basirun, & Centi, 2015). Furthermore, the energy level at the valence band is positive enough to oxidise the absorbed water molecules or hydroxyl ions, while the energy level at the conduction band is also negative enough to reduce absorbed molecular oxygen. Both aforementioned processes generate active surface radicals for degradation. In addition, the intrinsic band gap of TiO_2 is small enough for photoexcitation under UV light irradiation (Carp *et al.*, 2004). Based on Figure 2.2, the valence and conduction bands of other semiconductors, such as WO_3, Fe_2O_3, and Cu_2O do not lie within a strategic redox location as those observed for TiO_2, although their band gap is a lot smaller.

Apart from strategic band position and band gap values, an excellent photocatalyst should be non-toxic, photo-stable, and cost effective. In an aqueous environment, CdS and PbS semiconductor have been reported to undergo photo-corrosion and leaching of toxic heavy metals (Colmenares *et al.*, 2009). ZnO have almost similar band position and band gap as TiO_2, but it is unstable and readily dissolves in water, forming $Zn(OH)_2$ on ZnO particle surface (Chakrabarti & Dutta, 2004; Chen & Mao, 2007), which will deactivate the catalyst over time. Thus, TiO_2 is almost an ideal photocatalyst, as it is photo-stable, with energy bands strategically located for redox activity under UV light irradiation.

2.6 Design of TiO_2 as a photocatalyst

The remarkable physicochemical properties of TiO_2 has renewed interest in fields involving energy-conversion applications, such as photocatalysis, fuel generation, CO_2 reduction, electrochromic devices, and solar cells (Carp *et al.*, 2004; Zaleska, 2008). Contrarily, the application of conventional TiO_2 for practical and commercial perspectives remains limited, particularly in photocatalysis, due to a band gap of 3.2 eV for anatase TiO_2 (Asahi *et al.*, 2014). The photocatalytic activity of TiO_2 is a surface-driven catalytic mechanism, and the rate is influenced by the concentration of surface radicals, such as hydroxyl radicals ($\cdot OH$) and superoxide anion radicals ($\cdot O_2^-$) (Gaya, 2014; Zaleska, 2008). Thus, the mobility of charge carriers towards the catalyst surface and the ability of the catalyst to absorb photons needs to be taken into account when designing TiO_2 (H. Park *et al.*, 2013).

2.6.1 Surfactant

The usage of surfactants to prepare mesoporous silica was first initiated by Mobil in 1992 (Luo *et al.*, 2003). Similar analogy is introduced in preparing mesoporous TiO_2 which significantly affects the morphology, size, porosity, and surface area. TiO_2 prepared without surfactants results in poorly structured materials due to dense inorganic chains from less-controlled hydrolysis and condensation (Shahini *et al.*, 2011). The preparation of TiO_2 using alkyl phosphate surfactant via sol-gel initiated by Antonelli & Ying (1995) sparks interests as an alternative approach towards enhancing the properties of TiO_2. Since then, various surfactants were used, such as phosphates, ionic surfactants, non-ionic surfactants, amines, and block co-polymers to prepare TiO_2 (Agarwala & Ho, 2009; Antonelli & Ying, 1995; Deng *et al.*, 2013). In another work, cetyltrimethylammonium bromide (CTAB) was used to prepare TiO_2, which resulted in increased surface area and crystallinity (Peng *et al.*, 2005). The addition of pluronic F127 during the sol-gel process does not affect the final pH of the solution, therefore, the rate of hydrolysis and condensation remains unaffected (Mahshid *et al.*, 2007).

2.6.2 Cation and anion doping

TiO_2 doped with transition metals such as Cr, Fe, Ni, Cu, V and Mn, have been used to promote the visible light absorption (Choi *et al.*, 1994; Pappa *et al.*, 2015; Zhou *et al.*, 2006). Among the transition metals, vanadium-doped TiO_2 in low concentrations demonstrated better photocatalytic efficiency due to the increased lifetime of the photogenerated charges and extended absorption range (Wu & Chen, 2004). V-doped TiO_2 was prepared using hydrothermal method and V_2O_5/ HCl as its metal precursor, from a concentration of 0.1 - 0.9 % (Thuy *et al.*, 2012). The catalyst reported a single anatase crystal phase and visible light absorption. The improved optical response was attributed to the formation of lattice disorders and charge-transfer transitions from the d-d orbitals of vanadium to the conduction band of TiO_2. It has been widely reported that for metal-doped TiO_2, the Fermi level within TiO_2's band gap shifts towards the valence band, where the effective mass is the lowest (Siddhapara & Shah, 2014). This leads to an alteration on the intrinsic band gap of TiO_2, which increases the range of light absorption.

Doping TiO_2 with non-metallic anion such as N, F, S, and C replaces O in the TiO_2 lattice to create energy levels above the top of the valence band of TiO_2 to effectively narrow the band gap (Asahi *et al.*, 2014; Zaleska, 2008). Out of all non-metal doping, doping with nitrogen has been reported to result in the best photocatalytic activity (Ananpattarachai *et al.*, 2009). It was also showed that low and high nitrogen loading favoured interstitial and substitutional TiO_2 doping, respectively. Contrary to cationic doping (i.e. transition metals), anionic doping does not form deep localised d states which acts as charge recombination centres (Asahi *et al.*, 2001). Nitrogen doping is also widely reported to induce red optical shift towards visible light. One possible reason is the overlapping of O 2p and N 2p energy levels and the subsequent narrowing of the band gap (Samsudin, Hamid, Juan, Basirun, Kandjani, *et al.*, 2015)

2.6.3 Co-doping

The idea of combining two dopants for the preparation of co-doped TiO_2 has gained attraction as an alternative to improve towards improving photocatalytic activity (Jusof Khadidi *et al.*, 2013; Zaleska, 2008). Co-doping can be achieved using transition metal and non-metal dopants, lanthanoids, and non-metal dopants or two non-metal dopants. For example, the synergy between nitrogen and fluorine in N, F co-doped TiO_2 facilitates superior visible light photocatalytic activity due to modified colour centre, smaller band gap, enhanced crystallinity, oxygen vacancies, larger surface area, and the inhibition of electron and hole recombination (Samsudin, Hamid, Juan, Basirun, & Centi, 2015).

In other works, Ce, N co-doped TiO_2 was prepared using sol-gel method and demonstrated improved photocatalytic activity, surpassing the performance of non-doped and N-doped TiO_2 (C. Liu *et al.*, 2008). This observation is attributed to the significant optical response to 500 nm (visible light) and also, additional presence of active sites (Ti^{3+}) on the catalyst surface.

2.6.4 Other modification

Band gap engineering to achieve for wider solar light absorption can be achieved by nano-compositing TiO_2 with another metal oxide or semiconductor such as Cu_2O, ZrO_2, SiO_2, Al_2O_3, WO_3, SnO_2, and many more (Hu, Lu, Chen, & Zhang, 2013; Zaleska, 2008).

2.7 Synthesis of titanium dioxide nanoparticles

Recently, numerous synthesis methods of TiO_2 have been introduced, including sol-gel, hydrothermal, solvothermal, chemical vapour deposition, spray pyrolysis, electrochemical, sonochemical, and microwave methods (Malekshahi Byranvand *et al.*, 2013). Different synthesis method affects the nucleation and growth of TiO_2 and properties such as morphology (nanoparticles, nanorods, nanotubes, nanoflakes, nanoflowers), size, particle uniformity, crystal structure, and surface reactivity (active sites such as defects and facets) (Wang *et al.*, 2014). Powdered nanoparticles are generally prepared by sol-gel, hydrothermal and solvothermal method, while thin films and nanotubes can be prepared by chemical vapour deposition. The microwave method can be used to compliment the conventional preparation method; however its sensitivity towards the change in the physical and chemical properties of TiO_2 also needs to be addressed.

2.7.1 Sol-gel method

Nano-sized TiO_2 is commonly prepared using room temperature sol-gel method, as allows for efficient control of its purity, homogeneity and composition (Su *et al.*, 2004). According to Paul and Choudhury (2013), tailoring of certain TiO_2 properties such as morphology, size, and porosity is indeed possible via the sol-gel method in solution. Moreover, the sol-gel method does not require any special equipment (Padmanabhan *et al.*, 2007). TiO_2 prepared using the sol-gel method is shown to demonstrate high photocatalytic activity as well (Santana-Aranda *et al.*, 2005). Vijayalaxmi & Rajendran, (2012) reported smaller particle sizes with better crystallinity by TiO_2 using sol-gel relative to the hydrothermal method, prepared in similar conditions.

In a sol-gel method, the physico-chemical properties of TiO_2 are greatly influenced by the type and ratio of titanium precursor, solvent, water, and pH condition, thus affecting the rate of hydrolysis and condensation. The steps in sol-gel procedure are as following below.

Hydrolysis:

$$\boldsymbol{M(OR)_n + H_2O \rightarrow M(OR)_{n-1}(OH) + ROH}$$

Condensation:

$$\boldsymbol{M(OR)_n + M(OR)_{n-1}(OH) \rightarrow M_2(OR)_{2n-n} + ROH}$$

Poly-condensation:

$$\boldsymbol{2M(OR)_{n-1}(OH) \rightarrow M_2(OR)_{2n-n} + H_2O}$$

Overall Reaction:

$$\boldsymbol{M(OR)_n + (n/H_2O) \rightarrow MO_{(n/2)} + nROH}$$

Although the sol-gel method is advantageous, slight changes in the experimental conditions would yield different catalytic properties. Thus, special care should be taken during the sol-gel process when reproducing TiO_2 using this method.

2.7.2 Hydrothermal method

Different from the sol-gel method, the preparation of TiO_2 using the hydrothermal method is conducted in a closed system (steel pressure vessels autoclaves with or without Teflon liners) under controlled pressure ($P < 10$ mPa) and temperature ($T < 200$ °C) using aqueous mixture as the solvent. The type of aqueous solvent includes deionised water, NaOH and inorganic salts (Wang *et al.*, 2014). The pressure during the hydrothermal process is greatly influenced by the operating temperature and type of solvent used (Malekshahi Byranvand *et al.*, 2013). The process includes crystal growth and transformation, phase equilibrium and the formation of fine nanocrystals (Wang *et al.*, 2014).

Different pH enables the tuning of TiO_2 shapes, which includes nanoparticles, nanorods, and nanotubes during the hydrothermal process (Malekshahi Byranvand *et al.*, 2013). The hydrothermal method also produces TiO_2 with consistent homogeneity, purity, and particle sizes (Kitano *et al.*, 2007). A typical hydrothermal process would require mixing the titanium precursor with the selected solvent, and treating it in an autoclave at high temperatures. The obtained precipitate is then washed with deionised water and dispersed in acid prior to undergoing, calcination to form well-defined nanoparticles of TiO_2 (Wang *et al.*, 2014).

2.7.3 Solvothermal method

The solvothermal method is almost similar to the hydrothermal method, except that non-aqueous organic solvents are used instead of water-based solvents. Organic solvents include alcohol, toluene, acetone, and carboxylic acid (Wang *et al.*, 2014). Thus, higher temperatures and pressures is possible with this method. The solvothermal method also showed better catalytic properties relative to hydrothermally prepared TiO_2 with respect to size, uniformity, agglomeration and crystal phase (He *et al.*, 2012).

Furthermore, calcination of the catalyst is unnecessary, as crystalline TiO_2 is readily formed during the dissolution-precipitation process in the autoclave chamber. Highly crystalline TiO_2 was obtained using the solvothermal method due to the low dielectric constant of the organic solvents. This give rise to a decreased solubility of the TiO_2, which limits the dehydration process, and the formation of smaller highly crystalline nanoparticles (Lucky *et al.*, 2010).

2.7.4 Chemical vapour deposition (CVD) method

The preparation of TiO_2 thin films by condensing heated gas and depositing it as solid film on a hot substrate is achieved by the chemical vapour deposition method (CVD). This method is normally used to form surface coatings of various materials to improve its mechanical, electrical, optical, resistivity, and thermal properties (Wang *et al.*, 2014). The properties of TiO_2 thin films prepared by the CVD are controlled by the gas flow rate and composition, temperature, pressure and chamber geometry. A more enhanced CVD process would involve the use of ions, photons, plasmas, lasers or combustion reactions to increase solid deposition rates (Warwick *et al.*, 2011).

2.7.5 Microwaves-assisted method

Microwave-assisted method is a highly productive rapid synthesis technique via homogeneous heating, which requires a less stringent process conditions relative to other conventional synthesis methods that requires complex chemical mixtures and longer reaction times. Microwaves are a form of electromagnetic radiation, with principal frequencies of microwave heating between 900-2450 MHz (Wang *et al.*, 2014). The low production cost, coupled with high energy conversion efficiency, results in greater interests in using microwave-assisted method for dye-sensitised solar cells application to replace conventional silicon-based solar cells (Wang *et al.*, 2011). The microwave method can be used alongside hydrothermal and solvothermal processes by inducing localised and uniform heating in the autoclave, rather than heat being transferred from the autoclave wall to the liquid mixture, which requires longer processing times.

2.8 Application of TiO_2 for water treatment

The photocatalytic degradation of toxic wastes in contaminated water has been intensively studied using various forms of TiO_2, which includes nanopowders, nanotubes, and thin film TiO_2 deposited (Wang *et al.*, 2014). Removing toxic substances in contaminated water via photocatalytic degradation increases water reusability and environmental sustainability, particularly in the case of aquatic species. Furthermore, the removal of harmful materials in drinking water sources makes it safe to consume. The advantage of using TiO_2 is that the photodegradation process generally leads to the formation of harmless minerals, CO_2, and H_2O (Gaya, 2014). TiO_2 is highly effective in degrading organic pollutants, such as dyes and its application are further elaborated in **section 2.8.1.**

There are many parameters that affect the photocatalytic degradation activity in an aqueous system, which includes the type of photocatalyst, initial pollutant concentration, catalyst loading, medium pH, dissolved and aerated oxygen concentration, Fenton reagents, light intensity and wavelength, and spectators' component (impurities). Optimisation of these degradation parameters has been the focus of various photodegradation studies to design an effective and sustainable treatment process (Ahmed *et al.*, 2010). For photocatalytic degradation of dyes, high initial dye concentration limits the formation of $^{\cdot}OH$ radicals on the catalysts' surface. This is due to the adhesion of larger quantity of dyes covering the active sites of the catalyst and reducing the formation of radicals from the oxidation of absorbed surface hydroxyls. The path length for photons to diffuse through the dyes molecules and reaching the catalyst surface for photoexcitation also decreased, and vice versa (Neppolian *et al.*, 2002).

2.8.1 Photocatalytic degradation of dyes

The photocatalytic degradation of dyes has been used to sanitise dye polluted water (Bhatkhande *et al.*, 2002). This strategy differs from more time consuming biological methods, such as microbial degradation, adsorption by microbial biomass, dye decolourisation, and bioremediation. In photocatalytic degradation of dyes, the pollutant is rapidly degraded with the aid of UV or solar light irradiation.

As dyes are anionic and cationic, the isoelectric point (IEP) of the photocatalyst plays an important role that influences the overall photocatalytic activity. For most TiO_2 photocatalyst, the reported IEP is at a pH of 6.4 (Du Pasquier *et al.*, 2009). Thus, the absorption onto TiO_2 surface for anionic (negatively charged) and cationic (positively charged) dyes are favoured at acidic and alkaline environment, respectively.

The applications of bare and modified TiO_2 towards the photocatalytic degradation of the dyes pollutant are shown in Table 2.3.

Table 2.3: Using TiO_2 for the removal of dyes in contaminated water

Photocatalyst	Light irradiation	Dye	Photocatalytic efficiency	Modification effect	Reference
Commercial Degussa P25	Solar light	Reactive blue 4	~ 98 % dye removal at 1 x 10^{-4}M dye concentration in 24 h	• None	(Neppolian *et al.*, 2002)
Vanadium doped TiO_2	Sunlight (11.00 am – 3.00 pm)	Methylene blue	> 90 % degradation of MB in 5 hours	• V^{4+} creating trapping centre while V^{5+} e^- acceptor • Increase porosity of material.	(Shao *et al.*, 2015)
	Hg-medium lamp (λ > 420 nm)	Methylene blue	> 80 % of MB degradation in 6 min	• Hinders transformation of anatase to rutile • Red shifted • Acting as electron-hole trapping centre	(Khan & Berk, 2013)
Nitrogen doped TiO_2	Halogen bulb (λ > 420 nm)	Orange II	> 90 % of Orange II degradation in 4 hours	• Enhance light absorption in visible region	(Chakrabortty & Gupta, 2015)
	Direct solar light	Reactive black 5 (RB5)	> 53 % of RB5 dye removal in 30 min and complete decolourisation in 240 min	• Enhance light absorption in visible region	(Liu *et al.*, 2005)

Table 2.3, continued

Modifier	Light irradiation	Dye	Photocatalytic efficiency	Modification effect	Reference
Nitrogen Sulfur co-doped TiO_2	18W low-pressure Hg lamp as UV-light and sunlight as UV-Vis light source	Methyl orange (MO)	Almost complete colour removal and dye mineralization is observed in 120 min (UV light) and 720 min (vis light) for N,S co-doped TiO_2	• S doping enhance oxygen and dye absorption • N triggered surface oxygen vacancies and visible light absorption • Synergy between N and S enhanced the photocatalytic activity of MO	(Ahmed *et al.*, 2010)
Silver Nitrogen co-doped TiO_2	Direct visible light ($\lambda > 420$ nm)	Methylene blue	>90% of MB degradation in 10 hours	• Shift to visible light absorption • Enhanced electron-hole pair's	(Khan *et al.*, 2015)

CHAPTER 3: MATERIALS AND METHODOLOGY

3.1 Introduction

In this study, TiO_2 nanoparticles were prepared via the sol-gel method in the presence of a non-ionic surfactant. Subsequently, the surfactant assisted TiO_2 based photocatalysts were modified by mono-doping and dual-doping using vanadium (V) and nitrogen (N) precursors. The physico-chemical properties of the prepared photocatalysts powder were determined using FESEM, EDX, BET, XRD, Raman, DRS, and XPS. The photocatalytic activity was also evaluated under solar light using methylene blue (MB) as a model pollutant. An overview of the work flowchart is shown in Figure 3.1.

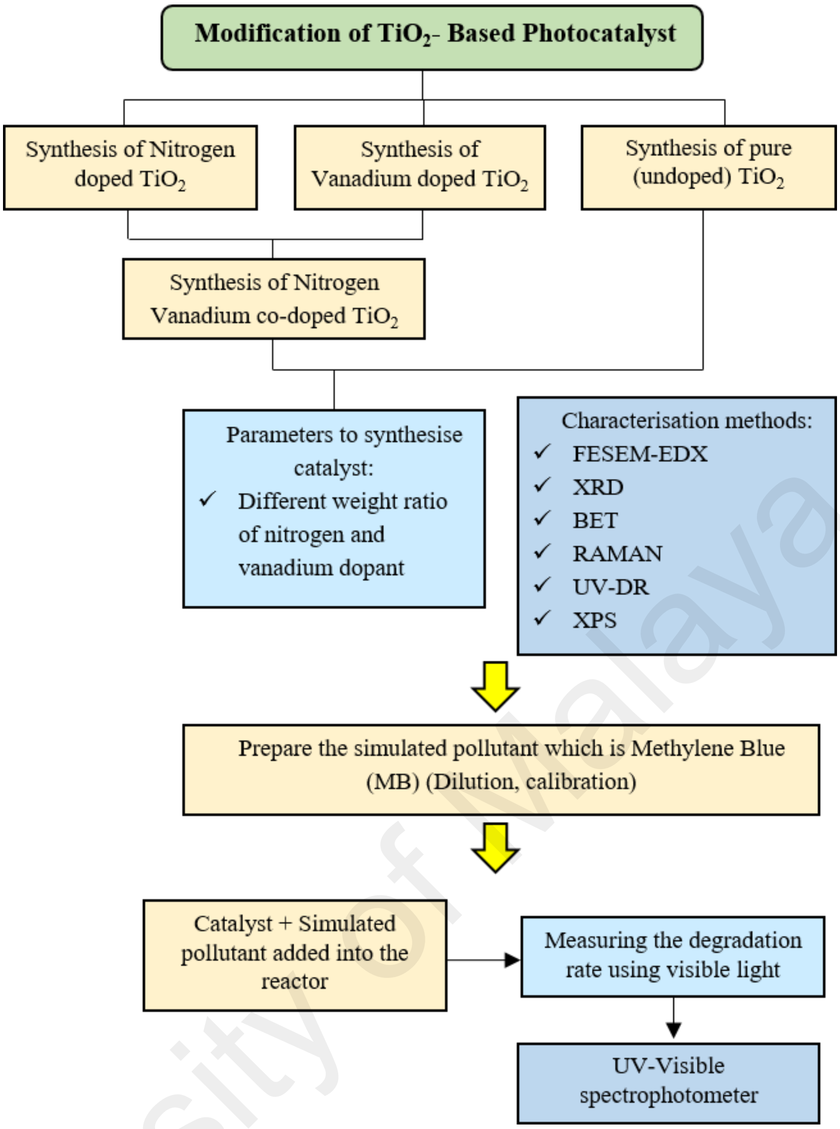

Figure 3.1: Overview of the research methodology

3.2 Materials and Chemicals

All of the chemicals used were purchased from Sigma Aldrich. Titanium isopropoxide (TTIP, 97 %), hydrochloric acid (HCl, 37 %), ethanol (95 %), absolute ethanol (99 %), ethanol and non-ionic surfactant pluronic F127 were used in the catalyst synthesis step. The source of nitrogen and vanadium precursors were triethylamine ($N(CH_2CH_3)_3$, 98 %), and ammonium metavanadate (NH_4VO_3, 99 %). Methylene blue (98 %) was used as a pollutant model to evaluate the photocatalytic degradation activity. Milli-Q deionised water was used throughout the experimental work.

3.3 Experimental methods

3.3.1 Stage 1: Synthesis of TiO_2, doped TiO_2 and co-doped TiO_2 nanoparticles

The precursor chemicals significantly influence the final crystallinity and crystal structure of TiO_2, which necessitates careful consistencies during synthesis. All of the TiO_2 based photocatalysts in this research work were prepared using the molar ratio tabulated in Table 3.1. This molar ratio was selected after optimisation process based on previous research (Samsudin *et al.*, 2015).

Table 3.1: Molar ration of prepared photocatalysts

Titanium Isopropoxide (TTIP)	Pluronic F127 surfactant	Hydrochloric acid (HCl)	Absolute ethanol	Deionised water
1	0.005	0.5	40	15

Table 3.2: Amount of chemical required using the weight percent (%) in Table 3.1 for the preparation of photocatalysis

Sample	Weight percent (%)
Undoped TiO_2	Without any dopant
Vanadium doped TiO_2	
V1-TiO_2	0.006
V2-TiO_2	0.125
V3-TiO_2	0.250
V4-TiO_2	0.500
V5-TiO_2	1.000
Nitrogen doped TiO_2	
N1-TiO_2	0.100
N2-TiO_2	0.250
N3-TiO_2	0.500
N4-TiO_2	0.750
N5-TiO_2	1.000
Vanadium Nitrogen co-doped TiO_2	
V2N4-TiO_2	0.125 (V) and 0.750 (N)

3.3.1.1 Undoped TiO_2 nanoparticles

Two types of mixtures were prepared; Mixtures A & B. The former consisted of absolute ethanol, and it was premixed with TTIP precursor for 5 min. Pluronic F127 powder was added into mixture A, and the mix was then stirred vigorously for 5 min until the pluronic F127 powders were dissolved. Mixture B consists of deionised water and hydrochloric acid. The pH of mixture B was kept at 3.5 ± 0.2 using HCl. Subsequently, mixture A was added drop-wised into mixture B while stirring, which results in the formation of a sol. The sol was aged at 45 °C overnight to form a cloudy white gel (Simonsen & Søgaard, 2010). The gel was washed several times using deionised water, followed by ethanol (95 %). The samples were dried at 70 °C for 16 h to remove any excess solvent (Simonsen & Søgaard, 2010), and it was then grinded into fine powder. To obtain nanoparticles TiO_2, the samples were calcined under continuous air flow at 450 °C for 2h.

3.3.1.2 Doped TiO_2 nanoparticles

For nitrogen doping, the weight per cent of nitrogen precursors are tabulated in Table 3.2. To prepare nitrogen doped TiO_2, trimethylamine ($N(CH_2CH_3)_3$) was added into mixture A. Mixture A consisted of absolute ethanol and F127, and it was premixed with the TTIP precursor for 5 min (Darzi *et al.*, 2012). Mixture B consisted of deionised water and hydrochloric acid. The pH of mixture B was kept at 3.5 ± 0.2 using HCl. Mixture B was added drop-wise into mixture A, which forms a sol. The ageing process involved the sample being stored for 24 h at 45 °C, followed by the gel being washed, dried, and calcined using the procedures outlined in **section 3.3.1.1**.

In other hand, for vanadium doping, ammonium metavanadate (NH_4VO_3) involved dissolving both constituents in mixture B, which consist of deionised water and HCl. This mixture was then added to the TTIP solution. Mixture B was added drop-wise into mixture A, which forms a sol (Shao *et al.*, 2015). The ageing process involved the sample being stored for 24 h at 45 °C, followed by the gel being washed, dried, and calcined using the procedures outlined in **section 3.3.1.1**.

3.3.1.3 Co-doped TiO_2 nanoparticles

To determine the molar ratio of vanadium and nitrogen required to prepare co-doped TiO_2, all single doped TiO_2 (vanadium-doped and nitrogen-doped) underwent photocatalytic reaction. The catalyst demonstrating the highest efficiency in dye degradation will be selected to synthesise co-doped TiO_2 (JiasongZhong *et al.*, 2014)

Vanadium nitrogen co-doped TiO_2 was produced by adding NH_4VO_3, deionised water, and the HCl mixture to $N(CH_2CH_3)_3$, F127, TTIP, and absolute ethanol solution, and the resulting solution is then vigorously stirred (Jaiswal *et al.*, 2012). The resulting solution was kept overnight at 45 °C for the gelation process. The ageing process involved the sample being stored for 24 h, followed by the gel being washed, dried, and calcined using the procedures outlined in **section 3.3.1.1**.

3.3.2 Stage 2: Characterisation of photocatalyst

Techniques such as XRD, BET, DRS, Raman, FESEM, EDX and XPS were used to elucidate the physico-chemical properties of the prepared photocatalysts. **Sections 3.3.2.1 - 3.3.2.7** outline the principle and analytical procedures of individual characterisation techniques.

3.3.2.1 X-ray Diffraction (XRD)

XRD is widely used to analyse the crystallinity, crystal phase, crystal ratio, planes and lattice spacing of any crystalline substance (Tsirelson & Ozerov, 1996).

XRD analysis was conducted using Bruker AXS D8 advanced diffractometer at 40 kV and 40 mA. The step size was 0.2° per second and Cu Kα radiation (α = 1.5406 Å) was used. The Bragg angle was analysed from 10° - 80°. Prior to the analysis, the sample was grinded into fine powder and closely packed into a sample holder. The samples' surface was homogenised using a non-leaching glass slide. The obtained XRD patterns were evaluated using High Score-Plus software, and the diffraction peaks were compared against the JCPDS standard reference patters. Spurr's and Scherrer's equations were employed to calculate the crystal phase ration and size, respectively.

Spurr's equation was used to determine the crystal ratio of individual phases in a mixed anatase/rutile TiO_2 (Spurr & Myers, 1957). The scattering coefficient used in this case was 1.26.

$$\boldsymbol{f_A = 1/(1 + 1.26\ x\ I_R/I_A)} \qquad \textbf{(Equation 3.1)}$$

Where, f_A = weight fraction of anatase,

I_A = intensity of maximum anatase phase peak (eg. 101)

I_R = intensity of maximum rutile phase peak (eg. 110).

Scherrer's equation was used to determine the crystallite size of nanoparticles of TiO_2 crystals, although it is not applicable for grains larger than 0.01 to 0.02 μm (Patterson, 1939).

$$\tau = \mathbf{K\,\lambda\ /\ ß\ cos\ \theta)} \qquad \textbf{(Equation 3.2)}$$

Where τ = mean size of the ordered (crystalline) domains

K = dimensionless shape factor,

λ = X-ray wavelength,

ß = line broadening at half the maximum intensity (FWHM)

θ = Bragg angle.

The dimensionless shape factor has a typical value of 0.9, but varies with the actual shape of the crystallite. The value of 0.9 generally represents spheres' particles, but is also valid for cubes, tetrahedral, and octahedral particles.

3.3.2.2 Brunauer-Emmet-Teller (BET)

BET is used to analyse textural properties, such as surface area, pore shape, pore size, and pore volume of the sample. The collected data is displayed as a BET isotherm, which plots the amount of gas adsorbed against the relative partial pressure. There are five types of adsorption isotherms: Types I, II, III, IV, and V (Giles *et al.*, 1974).

In this research, the textural properties of the samples were analysed using nitrogen adsorption-desorption analyser TriStar II 3020 series, Microactive 2.0. Prior to BET analysis, 1 g of the solid sample was dried in an oven at 60 °C for 2 h to remove any trapped moistures. The sample was then placed in a 6 mm glass cell and degassed in a vacuum chamber, operating at 350 °C for 6 h to remove any remaining moisture and potential contaminants. The sample was measured at a relative pressure range of 0.01-0.90 P/P_o.

3.3.2.3 UV-Vis Diffuse Reflectance Spectroscopy (DRS)

DRS are used to determine the optical properties of liquid and solid materials by quantifying the amount of absorbed and scattered lights.

DRS were conducted using Agilent Cary 100 model with a diffuse reflectance accessory. The sample was grinded into fine powder and packed firmly into a solid holder. The surface of the sample was homogenised using a glass slide. The sample was analysed using a double beam spectrometer. The lamp used was tungsten halogen, with light source between 190 - 900 nm. The slit width was fixed at 2 nm. The band gap of prepared TiO_2

was estimated using Kubelka-Munk's theory for powder samples. By plotting $[F(R_\infty)hv]\ 1/r$ versus hv, the intercept between the linear extrapolation of the graph and the baseline is the value of the band gap (eV). The reflectance function, F(R), was determined directly from the Agilent Cary 100 instrument, or can be calculated using Equation 3.1.

$$\boldsymbol{F(R_\infty) = (1 - R_\infty)\,2/2R_\infty = k/s} \qquad \textbf{(Equation 3.3)}$$

Where R = reflectance

k = absorption coefficient

s = scattering coefficient

h = Planck's constant

v = frequency.

The value of r used in this case was 2 for indirect allowed transition. Other r values include 1/2 (direct allowed transition), 3/2 (direct forbidden transition) and 3 (indirect forbidden transition). The band gap of the sample was determined using Kubelka-Munk function.

3.3.2.4 Raman Spectroscopy

Raman spectroscopy is generally employed to analyse the chemical structure of inorganic materials. It is based on the scattering of light by vibrating molecules as a result of the interaction between the monochromatic laser beam and the molecules of the sample. The Raman spectrum is constructed using scattered light, which has a different frequency from the incident light. This is referred to as inelastic scattering. The Raman spectra are formed due to the inelastic collision between the incident monochromatic beam and the molecules of the sample (Sushchinskiĭ, 1972).

Raman spectroscopy (Renishaw LabRam confocal Raman microscope with 325 nm line of a continuous He–Cd laser at room temperature) was used to analyse the chemical structure of the sample. The sample was grinded into fine powder prior to analysis.

3.3.2.5 Field Emission Scanning Electron Microscopy (FESEM)

In this research, FESEM Quanta FEI 200F was used to analyse the surface morphology, size, and particle distribution. The sample was dispersed in ethanol and sonicated in an ultrasonic bath at room temperature for 2 min to obtain a clear cloudy suspension. One drop was carefully fixed onto a carbon tape and was left to dry overnight in a desiccator prior to analysis. Both low (5 kV) and high (10 kV) voltages were employed to obtain the best resolution. The magnification was between 50 k -200 k.

3.3.2.6 Energy Dispersive X-ray (EDX)

Energy Dispersive X-ray (EDX), incorporated with FESEM instrument, is used to determine the elemental composition on the material's surface within a thickness of 500 nm. EDX is able to distinguish all elements in the order of 0.1 %, although it is limited to elements with atomic numbers greater than boron. X-rays are generated from the atoms when an electron beam from the FESEM scans across the sample's surface. The energy of the individual X-rays is characteristic of the elements that generate it (Joy & Romig Jr, 1986).

The elemental composition was determined using the INCA software, on a per area basis. The sample preparation for EDX analyses is similar to the sample preparation for FESEM imaging.

3.3.2.7 X-ray Photoelectron Spectroscopy (XPS)

X-Ray photoelectron spectroscopy, XPS is used to characterise the surface chemical state of a material from depths of 1 - 12 nm. The chemical element and nature of the chemical bonds between these elements can be detected, except in the case of hydrogen and helium. In XPS, the material is irradiated with sufficient energy of X-rays to excite the electrons away from the nuclear attraction force of an element into a vacuum state. In that state, the electron analyser measures the kinetic energy and produces an energy spectrum of intensity vs. binding energy. Each of the energy peaks on the spectrum represents a specific element (Chastain *et al.*, 1995).

The binding energy of different elements in the sample was determined using ThermoScientific K-alpha instrument. The sample was pressed into tablets prior to analysis using a non-monochromatised Mg K_α (photon energy of 1253.6 eV). A flat gold (Si/10nm Ti/200nm Au) was used as a substrate and reference. The XPS core levels were aligned to the C1s binding energy (BE) of 285 eV.

3.3.3 Stage 3: Photocatalytic Degradation of Methylene Blue (MB)

The photocatalytic reactor used was a stirred tank photo-reactor (STR) equipped with 100 ml pyrex tubes and a circulating water bath to maintain the temperature during the reaction. Solar visible light with a xenon arch lamp (150 W, Lux = 10,000, λ from 200 to 1000 nm) was used as a source of light.

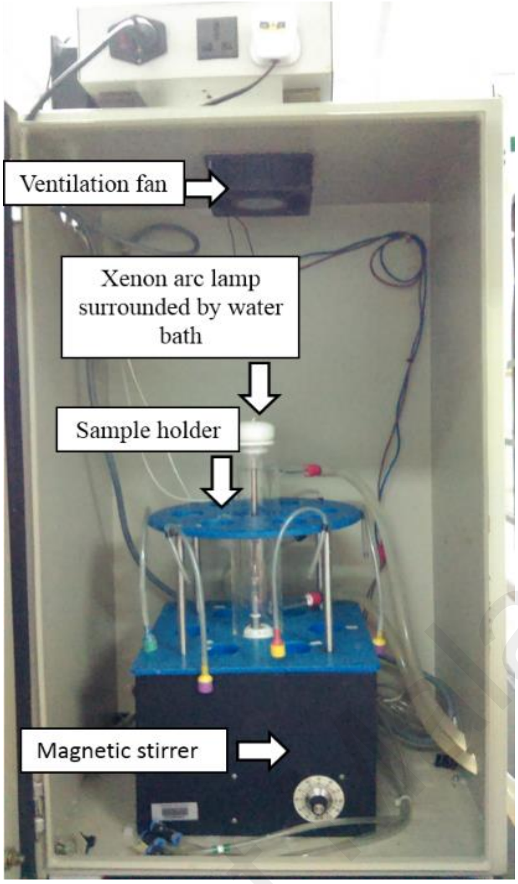

Figure 3.2: Schematic diagram of photocatalytic reactor setup

3.3.3.1 MB degradation percentage

The MB degradation percentage was calculated as follows (Zhou *et al.*, 2010);

$$\boldsymbol{D = \frac{(A_O - A)}{A_O} * 100} \qquad \textbf{(Equation 3.4)}$$

Where D = degradation percentage

A_O = absorbance of initial MB

A = absorbance of the solution after illumination

The measurement was repeated at two times for each photocatalyst drawn from one batch of material, and each result was averaged.

3.3.3.2 Rate constant of photocatalytic degradation of MB

The photocatalytic reactions rates are independent of hydroxyl concentrations (Guettai & Amar, 2005).Therefore a first-order kinetic model was used to fit the experimental data.

$$\frac{-dC_{MB}}{dt} = kC_{MB}C_{OH^*} \qquad \textbf{(Equation 3.5)}$$

Where, C_{MB} = dye concentration

C_{OH^*} = hydroxyl radical concentration

The rate expression **(Equation 3.5)** can fit an equation following the first order kinetics when C_{OH^*} is a constant in the presence of excess H_2O_2 (Guettai & Amar, 2005).

$$\frac{-dC_{MB}}{dt} = kC_{MB} \qquad \textbf{(Equation 3.6)}$$

$$\int_{C_{MB0}}^{C_{MB}} -dC_{MB} = k\int_0^t dt \qquad \textbf{(Equation 3.7)}$$

$$\ln(C_{MB0}/C_{MB}) = k \qquad \textbf{(Equation 3.8)}$$

Where, C_{MB0} = initial dye concentration

k = first order rate constant

C_{MB} = final dye concentration

CHAPTER 4: RESULTS AND DICUSSION

4.1 Undoped TiO_2 nanoparticles

The undoped TiO_2 synthesised were characterised using XRD, BET, DRS, Raman and FESEM.

4.1.1 X-ray diffraction (XRD)

X-ray diffraction was performed to investigate the nanostructured feature and crystallinity of TiO_2. Figure 4.1 shows the XRD patterns of synthesised undoped TiO_2 based on molar ratio (Table 3.1), indicating anatase phases with 11.40 nm as crystallite size. Undoped TiO_2 exhibited anatase peaks at 25°, 37°, 48°, 54°, 62°, and 68° correspond to the (101), (103), (200), (105), (213) and (116) planes. The peak of the synthesised undoped TiO_2 prepared by sol-gel was similar to the commercial TiO_2 (P25) (Theivasanthi & Alagar, 2013)

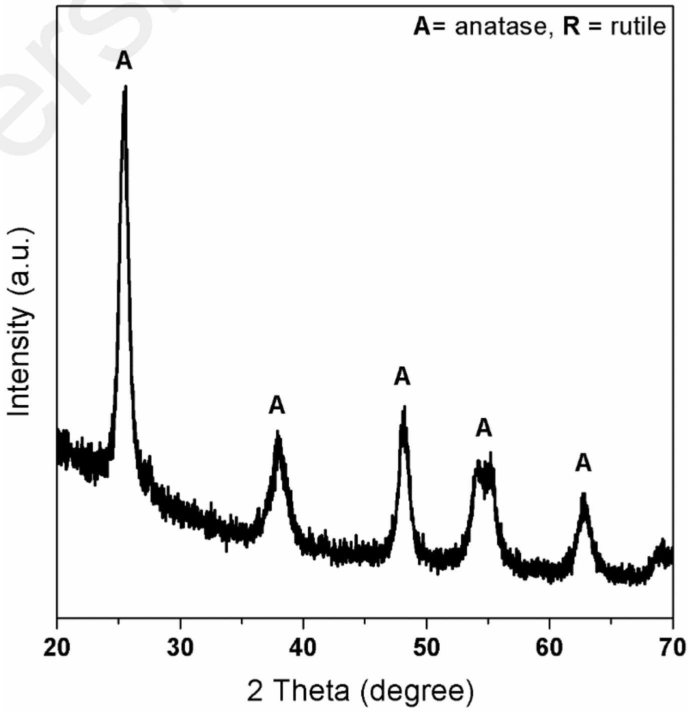

Figure 4.1: XRD curves of synthesised undoped TiO_2

4.1.2 Brunauer-Emmet-Teller (BET)

The specific BET surface area for the powder after the 450 °C heat-treatment was 102.89 m^2 /g. This surface area is higher than the ones reported in the literature for similar heat treatments (80.0 m^2 /g (Diebold, 2003) and 72 m^2 /g (K. S. Sing, 1985)) and is advantageous for the adsorption of a large amount of organic pollutant therefore, for light conversion efficiency improvement.

The adsorption-desorption isotherm of undoped TiO_2 is shown in Figure 4.2. The curve shape reveals a type IV isotherm behaviour. At relative pressure between 0.5 and 0.8, the curve exhibits a hysteresis loop (type H2) indicating a mesoporous texture of a solid consisting of agglomerates of spherical particles (Sing, 1985).

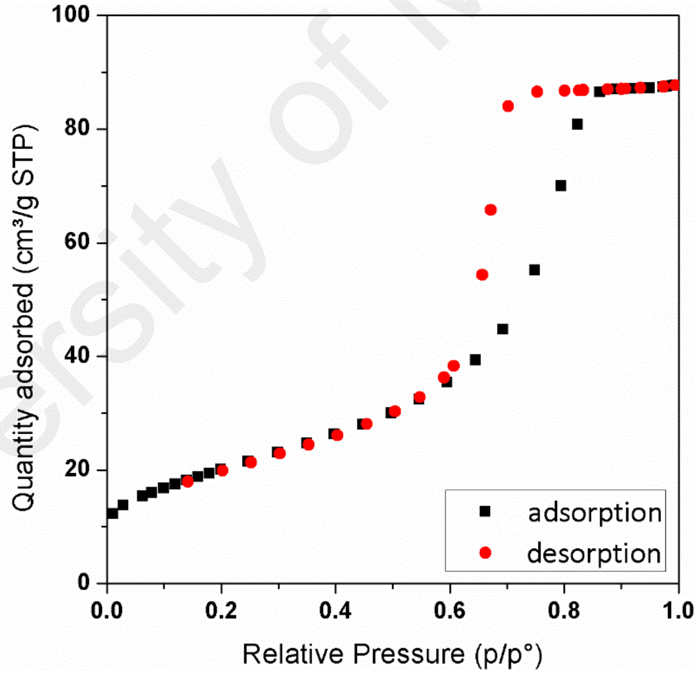

Figure 4.2: Nitrogen adsorption/desorption linear isotherms plot of synthesised undoped TiO_2

4.1.3 UV-Vis Diffuse Reflectance Spectroscopy (DRS)

DRS was used to study the electronic structure of the TiO_2 nanoparticles. The TiO_2 band-gap energy was determined by Kubelka–Munk model and the Tauc linearization (Figure 4.3). The optical band gap energies for synthesised undoped TiO_2 was 3.18 eV, in agreement with 3.20 eV referred in literature (Linsebigler *et al.*, 1995).

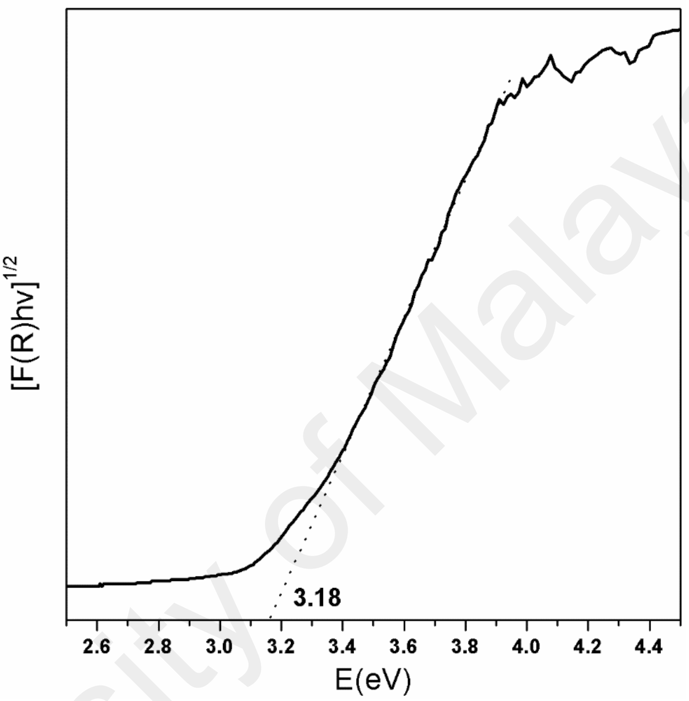

Figure 4.3: Kubelka-Munk function versus energy plots of synthesised undoped TiO_2

4.1.4 Raman Spectroscopy

Raman spectroscopy has been applied to characterise the obtained TiO_2 nanoparticles, the phase purity of the TiO_2 anatase was evident (Sushchinskiĭ, 1972), as the results shown in Figure 4.4. Anatase phase exhibit well distinct Raman finger print. The anatase structure is tetragonal. Its conventional cell is composed of two primitive one, each with two TiO_2 units. Six modes are A_{1g} (517 cm^{-1}), $2B_{1g}$ (395 cm^{-1} and 515 cm^{-1}) and $3E_g$ (144 cm^{-1}, 195 cm^{-1} and 637 cm^{-1}) are Raman active (Balachandran & Eror, 1982). In this research, the undoped TiO_2 nanoparticles show five anatase peaks at 144, 195, 395, 515 and 637 cm^{-1}, indicating the presence of TiO_2 anatase phase in accordance with above XRD results.

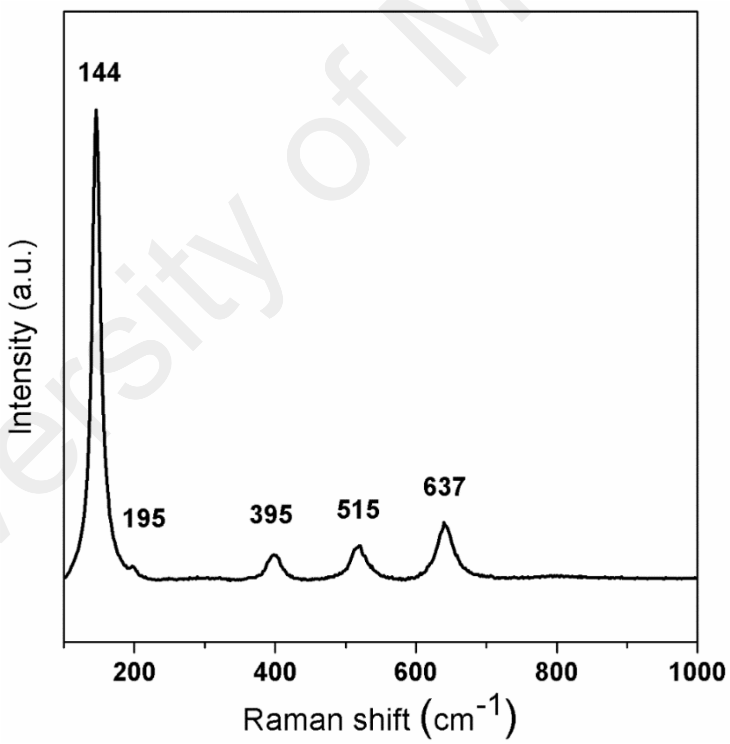

Figure 4.4: Raman spectra of synthesised undoped TiO_2

4.1.5 Field Emission Scanning Electron Microscopy (FESEM)

The structural study of the prepared undoped TiO_2 powder was studied using FESEM image analysis. The Figure 4.5 shows the FESEM images of synthesised undoped TiO_2 powder, which is heated at 450 ºC. The image as shown in Figure 4.5, particle was also found spherical in shape and surface morphology was found homogenous in specific regions. The agglomeration of the particles was seen in the FESEM images so that it shows the high degree of crystallinity of the TiO_2 nanoparticles (Park *et al.*, 2009).

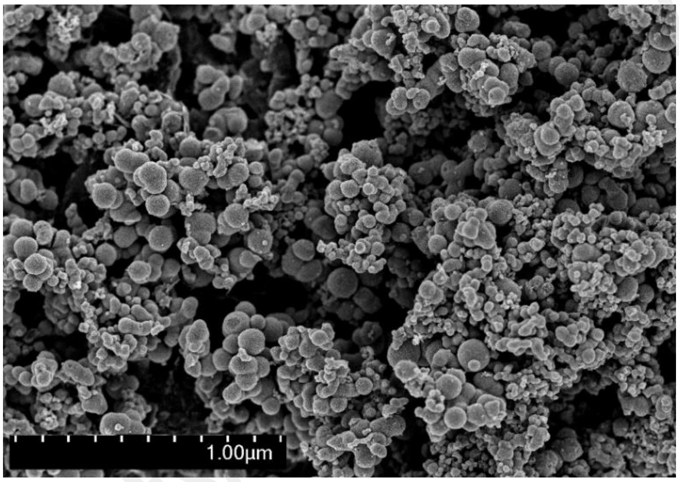

Figure 4.5: FESEM images of synthesised undoped TiO_2

4.2 Vanadium doped TiO_2 nanoparticles

The vanadium doped TiO_2 synthesised were characterised using XRD, BET, DRS, Raman, FESEM and EDX.

4.2.1 X-ray diffraction (XRD)

Figure 4.6 shows the XRD patterns of all vanadium doped TiO_2 with different molar ratios of V, indicating mixed anatase-rutile phases. Most samples exhibited anatase peaks at 25°, 37°, 48°, 54°, 55°, and 62°, while low concentration of dopants resulted in rutile peaks. Doping with metal oxides at a higher melting point than that of TiO_2 can inhibit the anatase-to-rutile phase transformation, while the opposite was observed when the melting point of the doping metal oxide is lower than that of TiO_2 (Ding *et al.*, 1996).

Based on this supposition, with increasing the vanadium loading, the intensity of anatase also increased, while for high vanadium loading samples, some rutile peaks disappeared (27°). Nevertheless, the fact that no vanadium phases (such as the V_2O_5 orthorhombic phase) were observed in the XRD spectra indicates that either vanadium was incorporated into the crystallite of TiO_2, or vanadium oxide was very small and highly dispersed (Doong *et al.*, 2009). As can be seen from Table 4.1, crystallite size was increased with increasing the vanadium loading on vanadium doped TiO_2 photocatalyst which accorded the results observed by Lin et al (2012) and the increasing of crystallite size leads to the decrease of specific surface areas in BET (Lin & Lin, 2012).

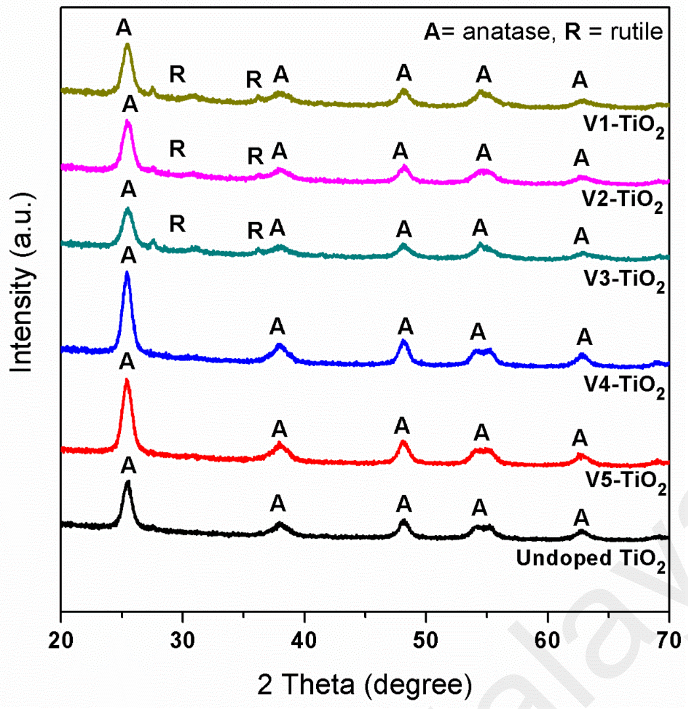

Figure 4.6: XRD curves of synthesised undoped TiO_2 and synthesised vanadium doped TiO_2

Table 4.1: Crystallite size, weight percent, and band gap of synthesised undoped TiO_2 and synthesised vanadium doped TiO_2

Sample	**Crystallite size (nm)**		**Weight percent (wt. %)**		**Band gap (eV)**
	Anatase	**Rutile**	**Anatase**	**Rutile**	
Undoped TiO_2	11.40	-	100	-	3.18
V1-TiO_2	10.4	27.2	76.6	23.40	2.90
V2-TiO_2	10.3	29.8	71.03	28.97	2.89
V3-TiO_2	10.9	32.0	67.07	32.93	2.96
V4-TiO_2	11.5	-	100	-	2.99
V5-TiO_2	12.9	-	100	-	3.07

4.2.2 Brunauer-Emmet-Teller (BET)

The textural properties of the photocatalysts were examined using nitrogen gas physisorption studies. The N_2 adsorption–desorption isotherms of the vanadium doped TiO_2 with different amounts of vanadium are shown in Figure 4.7, while Table 4.2 compares the resulting specific surface area of samples. The specific surface areas of all of the samples, including undoped TiO_2, exhibited type IV isotherms (Figure 4.8), signifying the presence of mesoporous structures associated with the capillary condensation of the adsorbent (Sing, 1985).

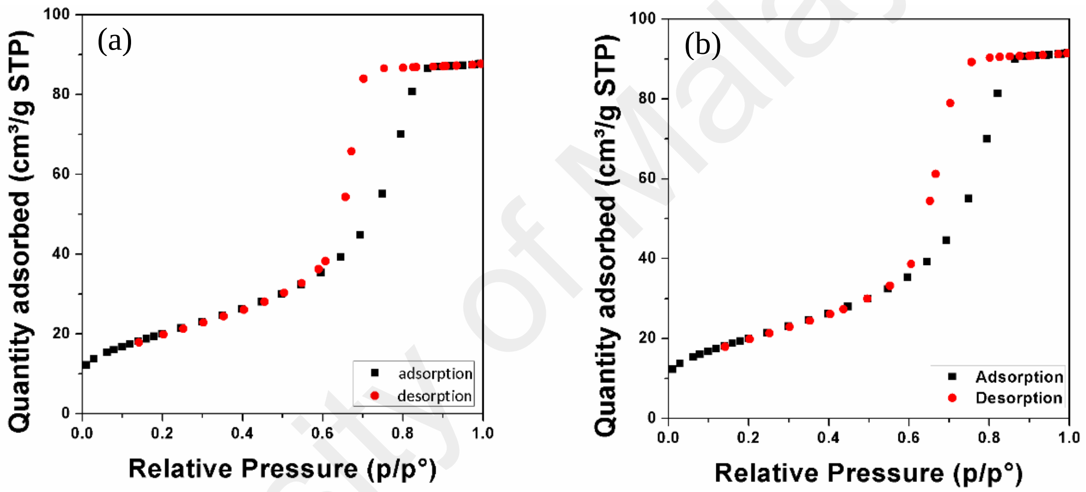

Figure 4.7: Nitrogen adsorption/desorption linear isotherms plot of synthesised (a) Undoped TiO_2 and (b) Vanadium doped TiO_2 (V2-TiO_2)

Table 4.2: Specific surface area and pore volume of synthesised undoped TiO_2 and synthesised vanadium doped TiO_2

Sample	Specific Surface area (m^2/g)	Pore volume (cm^3/g)
Undoped TiO_2	102.89	0.39
V1-TiO_2	75.82	0.20
V2-TiO_2	72.90	0.26
V3-TiO_2	72.88	0.28
V4-TiO_2	70.06	0.28
V5-TiO_2	61.05	0.30

4.2.3 UV-Vis Diffuse Reflectance Spectroscopy (DRS)

The optical properties of the samples demonstrate the remarkable shift of the absorption properties to low energy, where the band gap values of the TiO_2 samples is (~ 2.89 eV) (Figure 4.8) lower than that of the undoped TiO_2 (3.18 eV) (Table 4.1). The Eg exhibited by the vanadium doped TiO_2 samples shows that these samples can be activated by natural solar energy during the photodegradation of organic pollutants (Bañares *et al.*, 1996). The presence of vanadium ions significantly shifted the Kubelka-Munk spectra into the visible region and lower energy. This took place due to the appearance of new electronic states formed by vanadium in the TiO_2 band gap. Due to vanadium doping, impurity energy levels are created, which either overlaps with the valence band maximum or conduction band maximum of TiO_2 (Phung et al., 2015). Upon illumination, electrons in the valence band of TiO_2 are excited to the vanadium impurity energy level, then to the conduction band. This narrows the band gap, which extends the absorption spectrum towards the visible-light region.

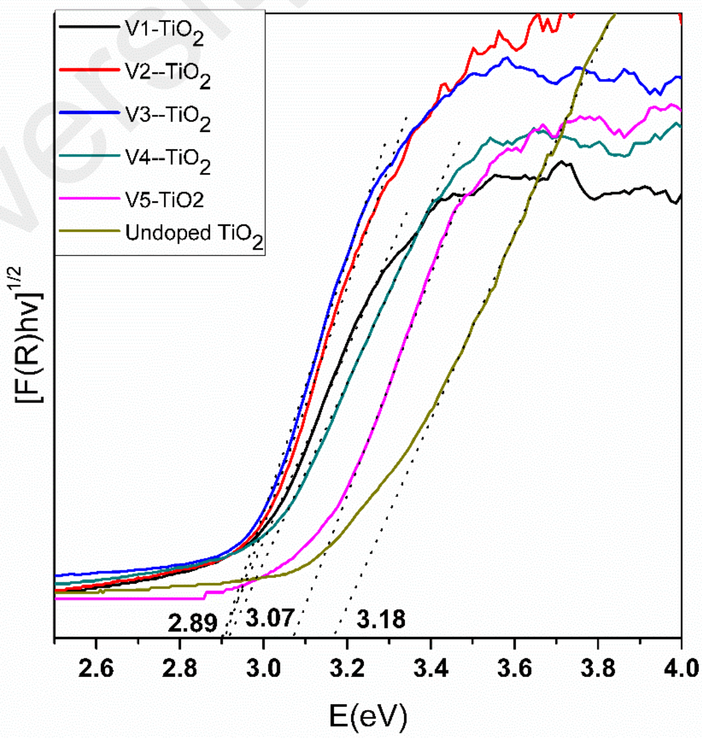

Figure 4.8: Kubelka-Munk function versus energy plots of synthesised undoped TiO_2 and synthesised vanadium doped TiO_2

4.2.4 Raman Spectroscopy

All of the prepared photocatalysts showed a significant anatase presence, with major bands at 144 cm^{-1} (E_g), 395 cm^{-1} (B_{1g}), 515 cm^{-1} (A_{1g}), and 637 cm^{-1} (E_{1g}) (Figure 4.9) (Yanagisawa & Ovenstone, 1999). This result is contrast with XRD result because XRD plots show some rutile peak at low concentrations of dopants, but the percentage of anatase exceeded that of rutile. This clearly indicates that the anatase crystal structure of the TiO_2 is stable even post-cation (V^{5+}/V^{4+}) doping (Klosek *et al*, 2001)

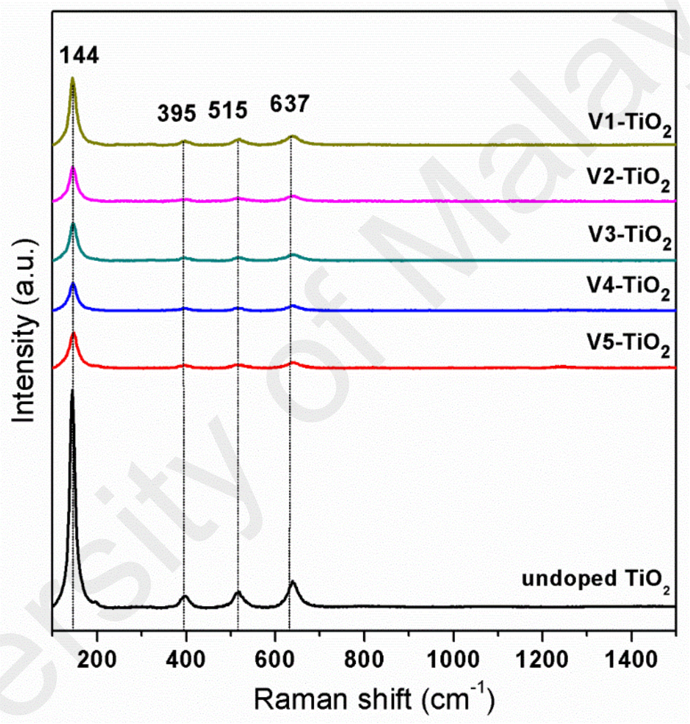

Figure 4.9: Raman spectra of synthesised undoped TiO_2 and synthesised vanadium doped TiO_2

4.2.5 Field Emission Scanning Electron Microscopy (FESEM)

Figure 4.10 shows the FESEM image of the surface texture of undoped TiO_2 (a) and vanadium doped TiO_2 sample (V2-TiO_2) (b). Although the XRD pattern does not show any peaks pertaining to V–Ti–O or V–O, which means that the dopant ions are uniformly dispersed into the TiO_2 crystallites (Khan & Berk, 2013). It is evident that grains of different shapes and sizes were obtained depending on many factors, such as synthetic route, calcination temperature, and V-to-Ti ratio (Avansi *et al.*, 2014). Initially, the undoped synthesised TiO_2 exhibited spherical aggregates (Figure 4.11(a)), but the aggregation behaviour of primary particles decreased upon calcination, leading to the formation of fine regular particles (Figure 4.11(b)) (Wu & Chen, 2004).

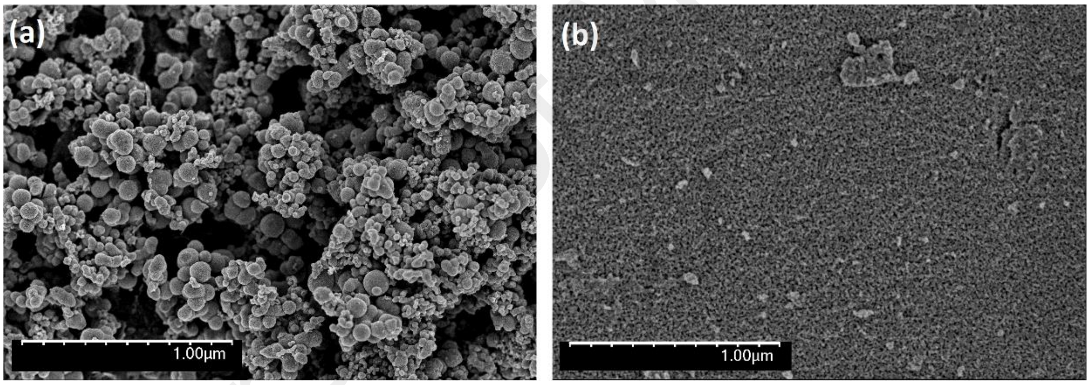

Figure 4.10: FESEM images of synthesised (a) Undoped TiO_2 and (b) Vanadium doped TiO_2 (V2-TiO_2)

4.2.6 Energy Dispersive X-ray (EDX)

The EDX results (Figure 4.11) of the representative sample of the Vanadium doped TiO_2 photocatalyst. The high weight percent of titanium and oxygen shows that they are the main components of the sample, at 72.80% and 27.08%, respectively. It was only 0.12 % for vanadium. Since the V was doped in low concentration (< 5 %), the tiny peak of V was overlapped with the bigger peak of Ti (Angeles-Chavez *et al.*, 2012)

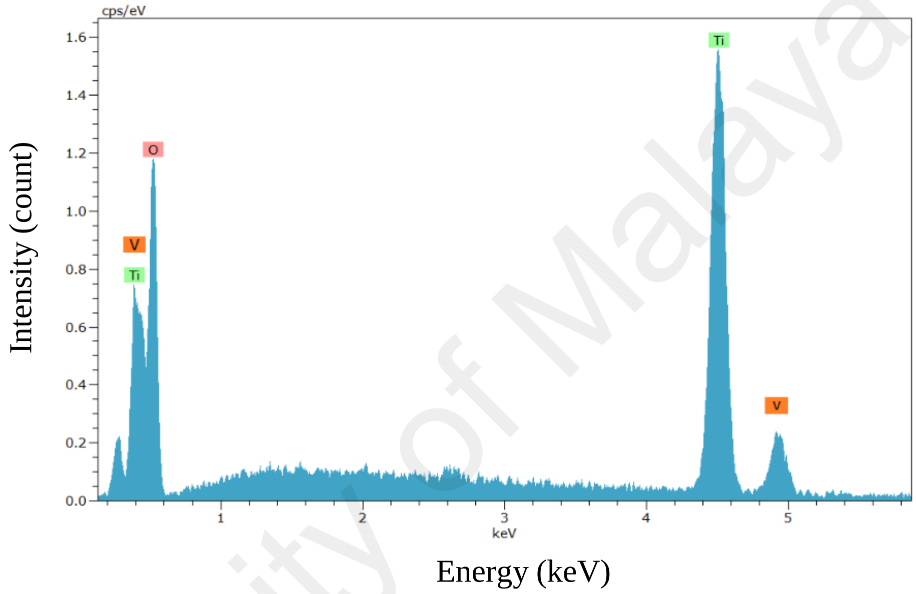

Figure 4.11: EDX spectra of synthesised vanadium doped TiO_2 ($V2-TiO_2$)

4.3 Nitrogen doped TiO_2 nanoparticles

The nitrogen doped TiO_2 synthesised were characterised using XRD, BET, DRS, Raman, FESEM and EDX.

4.3.1 X-ray diffraction (XRD)

Figure 4.12 shows the effect of nitrogen doping on the phase structure of TiO_2. The XRD patterns of all samples contained diffraction peaks at 25°, 37°, 48°, 54°, 55°, and 62°, which corresponds to the typical pattern of anatase TiO_2 (Figure 4.13). There is a small peak at 27°, which corresponds to the rutile phase being detected in N1-TiO_2 and N2-TiO_2 samples only (Liu *et al.*, 2005). Moreover, increased amount of nitrogen slightly increased the crystallinity of the materials. The width of the intense peak at $2\theta = 25°$ was used to determine the crystallite size of the materials. As listed in Table 4.3, the crystallite size of nitrogen doped TiO_2 were 11.40 – 25.26 nm for the anatase phase. The crystallite size of the materials was directly proportional to the nitrogen content in the materials (Eswar *et al.*, 2016).

Apparently, the introduction of nitrogen corralled the formation of the rutile phase, which means that there are more anatase phase in the nitrogen doped TiO_2. The presence of nitrogen in TiO_2 inhibits the condensation of the spiral chains of anatase TiO_6 octahedral to linear chains of rutile TiO_6 octahedral in the sol-gel process, while nitrogen improved the thermal stability of the catalyst by increasing the temperature required for the rutile phase formation (Samsudin, Hamid, Juan, Basirun, & Centi, 2015). Moreover, the presence of nitrogen in the TiO_2 lattice favours the formation of anatase due to the large ionic radius of N_3 compared to O_2 (Eswar *et al.*, 2016).

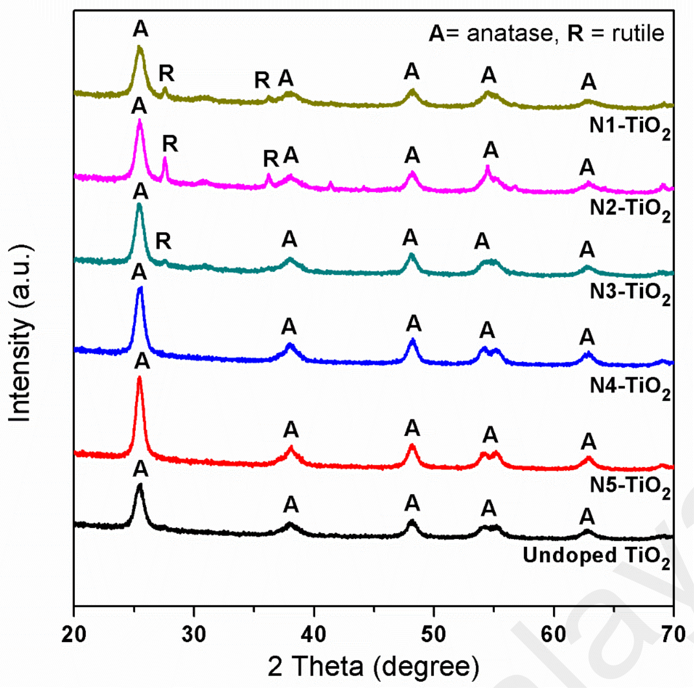

Figure 4.12: XRD curves of synthesised undoped TiO_2 and synthesised nitrogen doped TiO_2

Table 4.3: Crystallite size, weight percent, and band gap of synthesised undoped TiO_2 and synthesised nitrogen doped TiO_2

Sample	Crystallite size (nm)		Weight percent (wt. %)		Band gap (eV)
	Anatase	Rutile	Anatase	Rutile	
Undoped TiO_2	11.40	-	100	-	3.18
N1-TiO_2	15.27	26.86	79.15	20.85	2.93
N2-TiO_2	18.54	21.59	92.72	7.28	2.90
N3-TiO_2	19.09	-	100	-	2.91
N4-TiO_2	20.15	-	100	-	2.87
N5-TiO_2	25.26	-	100	-	2.95

4.3.2 Brunauer-Emmet-Teller (BET)

Specific surface area and porosity results presented in Table 4.4 showed that the decreasing of surface area when nitrogen loading increase. This happen because of the nitrogen increase the crystallite size of the particles (Liu *et al*, 2005) which is results was showed in XRD. The nitrogen absorption-desorption isotherms in Figure 4.13 demonstrated strong interactions of isotherm type IV and narrow distribution of uniform mesoporous pores between 2 - 50 nm (Sing, 1985).

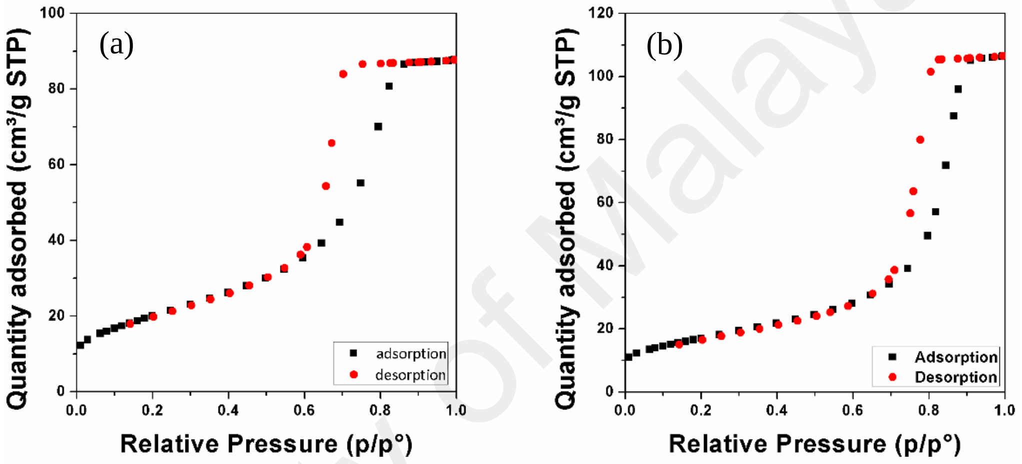

Figure 4.13: Nitrogen adsorption/desorption linear isotherms plot of synthesised (a) Undoped and (b) Nitrogen doped TiO_2 (N4-TiO_2)

Table 4.4: Specific surface area and pore volume of synthesised undoped TiO_2 and synthesised nitrogen doped TiO_2

Sample	Specific surface area (m^2/g)	Pore volume (cm^3/g)
Undoped TiO_2	102.89	0.39
N1-TiO_2	60.83	0.35
N2-TiO_2	55.07	0.27
N3-TiO_2	38.49	0.20
N4-TiO_2	30.83	0.22
N5-TiO_2	26.71	0.19

4.3.3 UV-Vis Diffuse Reflectance Spectroscopy (DRS)

Nitrogen doping slightly decreased the band gap to 2.87 - 2.95 eV (Figure 4.14). This was due to the impurity level created within the band gap, which shifts the Fermi level closer to the conduction band, thus narrowing the band gap (Asahi et al, 2001). This was further supported by Xiang et al (2011), whereby from the first principle density functional theory (DFT) calculation, the interstitial N-precursor induces local states above the valence band, and was responsible for visible light response. According to Tian et al (2012), substituting nitrogen in TiO_2 forms a narrow N 2p band, which overlaps the O 2p orbital, promoting greater electrons mobility from the valence band to the conduction band during photo-excitation.

In addition, the introduced oxygen vacancies resulted in a charge imbalance between O^{2-} and N^{3-} ions, which are also responsible for visible light absorption in Nitrogen doped TiO_2 (Chakrabortty & Gupta, 2015).

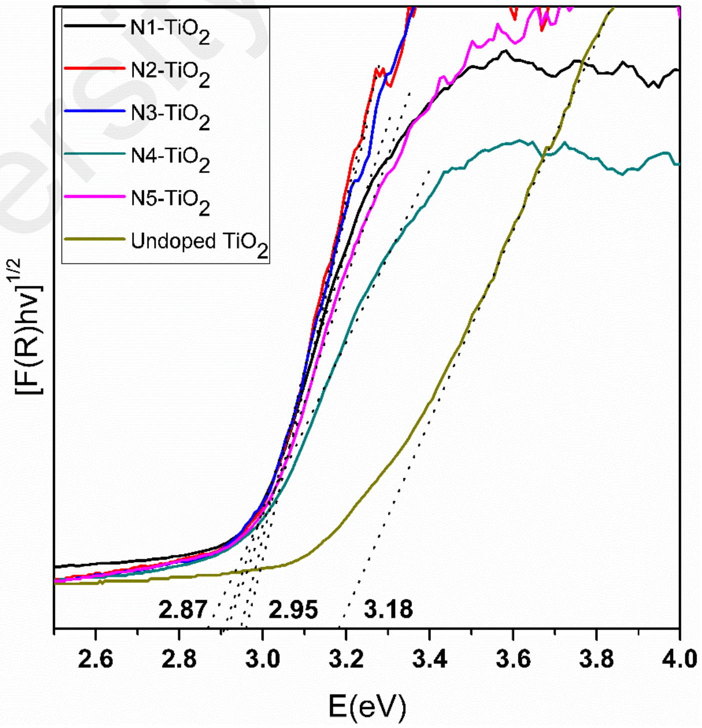

Figure 4.14: Kubelka-Munk function versus energy plots of synthesised undoped TiO_2 and synthesised nitrogen doped TiO_2

4.3.4 Raman Spectroscopy

All of the prepared photocatalysts are made up of the anatase phase (Figure 4.15), with major bands at 144 cm^{-1} (E_g), 395 cm^{-1} (B_{1g}), 515 cm^{-1} (A_{1g}), and 637 cm^{-1} (E_{1g}) (Figure 4.15) (Liu *et al*, 2005) similar with vanadium doped TiO_2. In all of the nitrogen doped TiO_2 samples, no significant rutile bands were observed at 446 cm^{-1} (E_g). Although the rutile phase was present in the most of the samples, as per the XRD curves, no significant rutile band are observed in the Raman spectra. This shows that Raman spectroscopy is suitable for identifying the presence of TiO_2, but not for distinguishing between anatase and rutile, especially at a low mass fractions (Ding *et al.*, 1996).

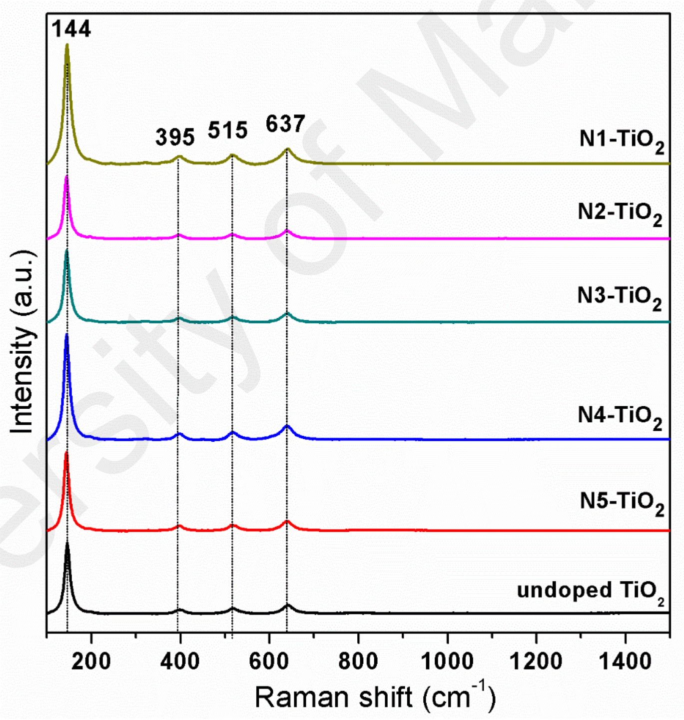

Figure 4.15: Raman spectra of synthesised undoped TiO_2 and synthesised nitrogen doped TiO_2

4.3.5 Field Emission Scanning Electron Microscopy (FESEM)

The FESEM images of undoped and nitrogen doped TiO_2 showed spherical particles with an average particle size of 27 - 37 nm (Figure 4.16). It can be seen that the nitrogen precursor has a minimal effect on the size and shape of the nanoparticles (Samsudin *et al*, 2015). Both samples show irregular crystal sizes, ranging from 11 - 25 nm, whereby larger crystallite sizes in XRD were observed in the doped TiO_2, due to the larger size of nitrogen atomic radius compared to the oxygen atomic radius in doped TiO_2, which slightly increase the particle size in nitrogen doped TiO_2 and decrease agglomeration (Asahi *et al*, 2014). This means that the homogeneity and dispersibility of the particles were enhanced. This observation contradicts a previous work, where a significant decrease in particle size was observed in nitrogen doped TiO_2 (Sathish *et al.*, 2005).

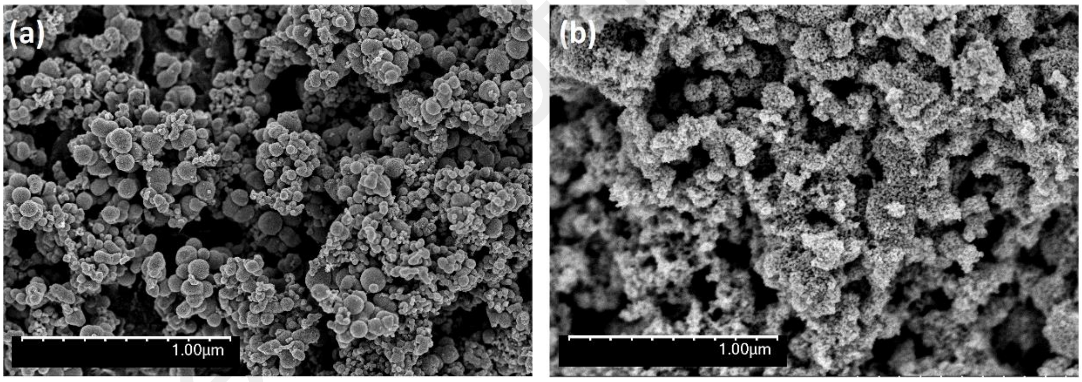

Figure 4.16: FESEM images of synthesised (a) Undoped TiO_2 and (b) Nitrogen doped TiO_2 (N4-TiO_2)

4.3.6 Energy Dispersive X-ray (EDX)

The EDX results (Figure 4.17) of the representative sample of the nitrogen doped TiO_2 photocatalyst confirmed the presence of Ti, N, and O elements. The high weight percent of titanium and oxygen shows that they are the main components of the sample, at 68.43 % and 30.82 %, respectively. We also observe large peaks for the elements of N and O, which slightly overlap each other with only 0.68 % for nitrogen. Figure 4.18 also shows that deconvolution of an EDX spectrum with peak overlaps between titanium and nitrogen. The width line was broadened due to the interaction effects in the detector and the electronic noise of the signal amplifiers (Berlin *et al.*, 2011).

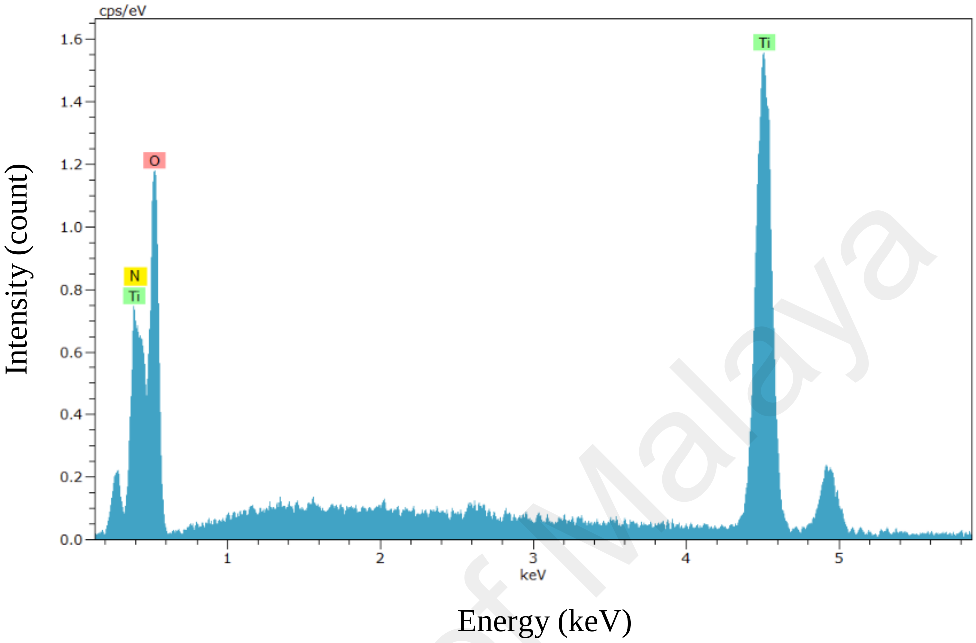

Figure 4.17: EDX spectra of synthesised nitrogen doped TiO_2 (N4-TiO_2)

4.4 Vanadium, Nitrogen co-doped TiO_2 nanoparticles

The vanadium nitrogen co-doped TiO_2 synthesised and characterised using XRD, BET, DRS, RAMAN, FESEM, EDX and XPS.

4.4.1 X-ray diffraction (XRD)

To identify the crystal structure of the synthesised photocatalysts, XRD patterns of the undoped TiO_2 and all of the compositions of doped and co-doped TiO_2 are shown in Figure 4.18. The presence of nitrogen in the TiO_2 lattice favours the formation of anatase due to the large ionic radius of N_3 compared to O_2. While, doping with vanadium (V^{4+}/V^{5+}) with ionic radiuses less than Ti, neutralises the charge and allows for the substitution of O_2 with N_3 in the TiO_2 lattice without distorting the TiO_2 structure (Rumaiz *et al.*, 2009). There were no peaks corresponding to oxides of vanadium and phase separation of TiO_2. Therefore, it can be assumed that vanadium ions have been completely substituted into the crystal lattice of TiO_2. (101), (004), (200), (211), and (204) are the planes found in all of the catalysts, which shows the absence of the rutile phase in all of the catalysts (Ding *et al.*, 1996). The width of the (101) peak shows broadening, while the intensity increases with increasing of the nitrogen and vanadium concentration. Stresses are created due to the difference in the bonding characteristics between nitrogen and oxygen. This replacement leads to a change in the electronic states and optical absorption (Xiangxin Yang *et al.*, 2009). Table 4.5 shows that the comparison of undoped, single doped and co-doped TiO_2 in term of crystallite size, weight percent and band gap.

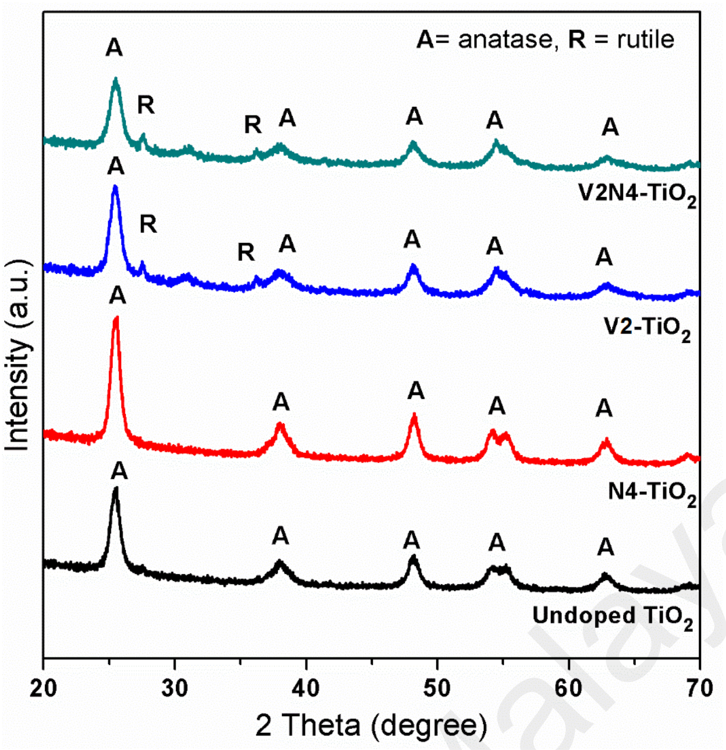

Figure 4.18: XRD curves of synthesised undoped TiO_2, doped TiO_2 and synthesised co-doped TiO_2

Table 4.5: Crystallite size, weight percent and band gap of synthesised undoped, doped and co-doped TiO_2

Sample	**Crystallite size (nm)**		**Weight percent (wt. %)**		**Band gap (eV)**
	Anatase	**Rutile**	**Anatase**	**Rutile**	
Undoped TiO_2	11.40	-	100	-	3.18
V2-TiO_2	13.25	32.00	71.02	28.98	2.89
N4-TiO_2	20.15	-	100	-	2.87
V2N4-TiO_2	24.18	13.3	76.89	23.11	2.65

4.4.2 Brunauer-Emmet-Teller (BET)

The specific surface area and porosity of undoped, doped, and co-doped TiO_2 was presented in Table 4.6 showed less influence on the change of porosity after nitrogen doping compared to the specific surface area. The nitrogen absorption-desorption isotherms in Figure 4.19 showed strong interactions of isotherm type IV and narrowed distribution of uniform mesoporous pores in the range of 2 - 50 nm (Sing, 1985; Xiang *et al.*, 2011).

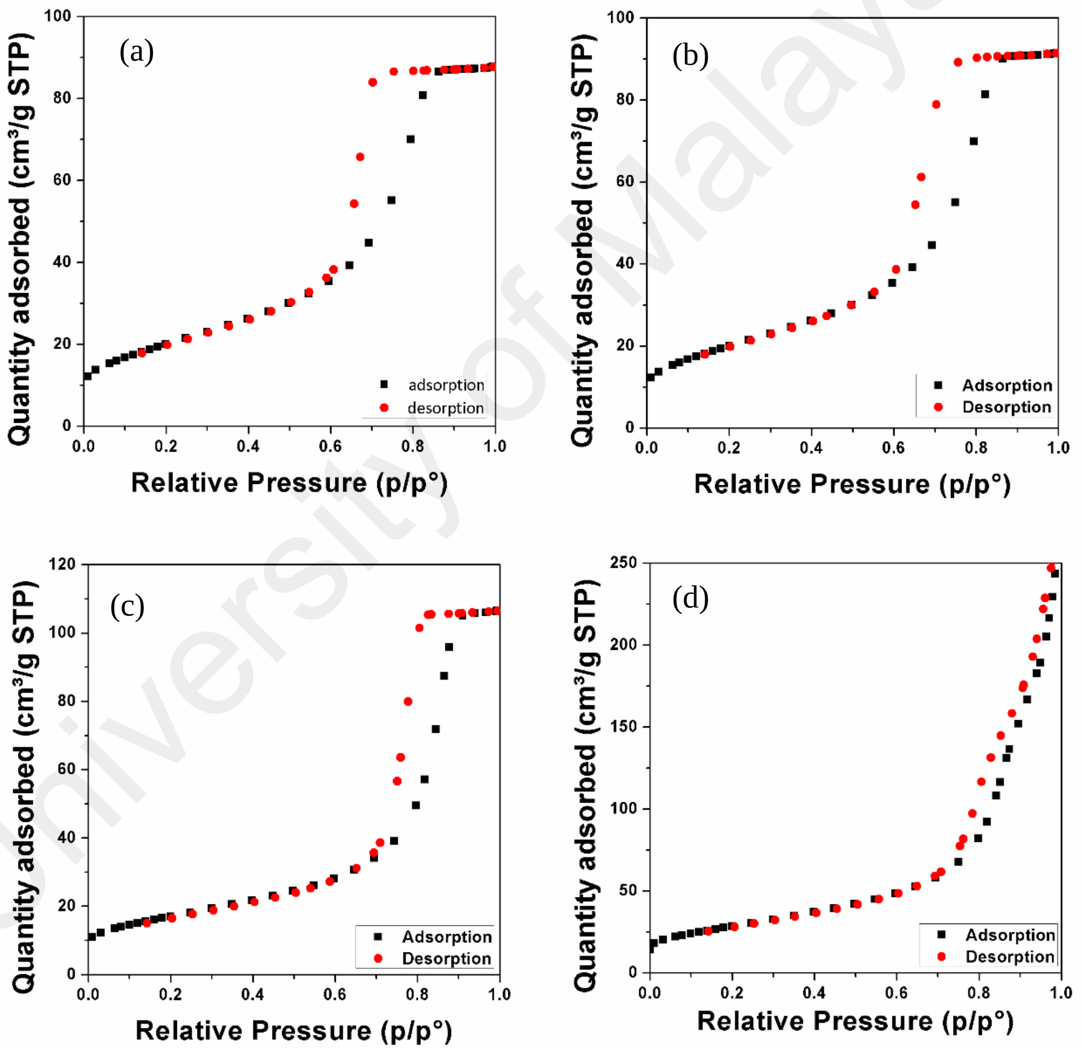

Figure 4.19: Nitrogen adsorption/desorption linear isotherms plot of synthesised (a) Undoped TiO_2 and (b) Vanadium doped TiO_2 (V2-TiO_2) (c) Nitrogen doped TiO_2 (N4-TiO_2) (d) Vanadium Nitrogen co-doped TiO_2 (V2N4-TiO_2)

Table 4.6: Specific surface area and pore volume of synthesised undoped, doped and co-doped TiO_2

Sample	Specific surface area (m^2/g)	Pore volume (cm^3/g)
Undoped TiO_2	102.89	0.39
N4-TiO_2	30.83	0.22
V2-TiO_2	72.90	0.26
V2N4-TiO_2	71.59	0.18

4.4.3 UV-Vis Diffuse Reflectance Spectroscopy (DRS)

The band gap of undoped TiO_2, V2–TiO_2, N4–TiO_2, and V2N4–TiO_2 co-doped TiO_2 were determined to be 3.18 eV, 2.89 eV, and 2.87 eV, and 2.65 eV, respectively, as shown in Figures 4.22. Single vanadium and nitrogen doping of TiO_2 significantly reduced the band gap by 0.29 eV and 0.31 eV, respectively, while the V and N co-doped TiO_2 resulted in the reduction of the band gap by 0.53 eV.

This indicates that co-doping of nitrogen and vanadium results in the creation of additional energy levels between the conduction and valence band edge of TiO_2 (Figure 4.20). This electronic transition from the dopant's electronic states to states of TiO_2 can effectively cause a red shift in the band edge absorption threshold (Cheng *et al.*, 2012) (Figure 4.21). The co-doping with nitrogen and vanadium induces the narrowing of the band gap of TiO_2. The metal ion implanted TiO_2 overlaps the conduction band of the d-orbital of TiO_2 (Choi *et al.*, 1994).

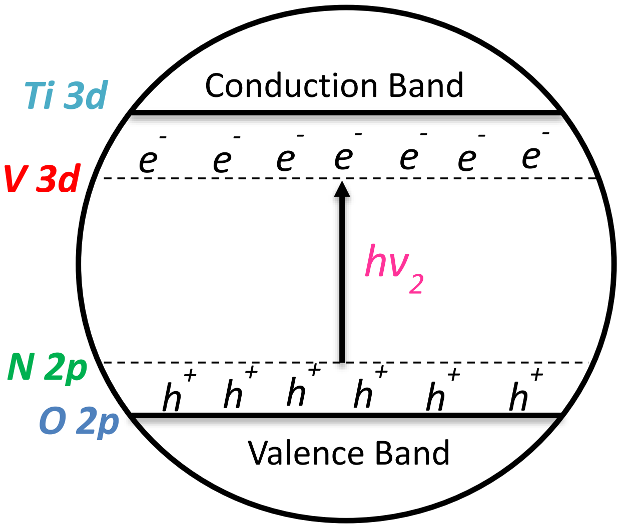

Figure 4.20: Schematic diagram for formation new impurity level of conduction band (V 3d) and valence band (N 2p) after TiO_2 was co-doped with nitrogen and vanadium

It can be suggested (Figure 4.21) that d-orbital overlapping from the dopant and parent lattice decreases the band gap of TiO_2 and enhances visible light absorption. 3d states of vanadium can occupy just below the conduction band of TiO_2 (Wu & Chen, 2004). Vanadium existing in V^{4+} and V^{3+} states, and electronic transition between these states can significantly enhance the absorption, narrowing the band gap (Avansi *et al.*, 2014). Furthermore, it is well known that nitrogen doping can form new states that lie just above the valence band for the substituted nitrogen. However, for the interstitial nitrogen, the N–O bond generates localised states with p-orbitals (Di Valentin *et al.*, 2005). This state lies below the O 2p band of TiO_2. This prevents additional states for the excited charge carriers and can prevent recombination. Therefore, nitrogen and vanadium doping resulted in the formation of new states close to the valence band and conduction band, respectively.

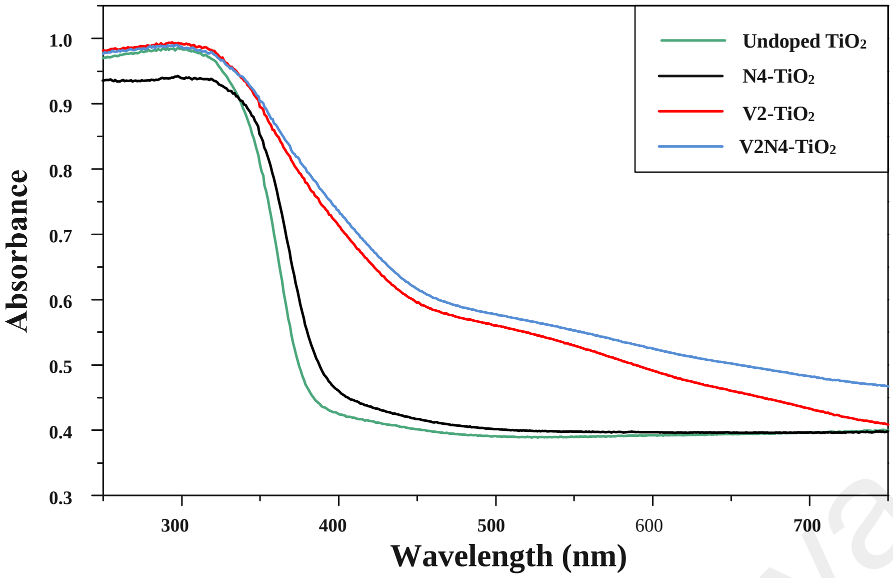

Figure 4.21: UV–Vis absorption spectra (diffuse reflectance), of synthesised undoped, vanadium doped, nitrogen doped TiO_2 and vanadium nitrogen co-doped TiO_2

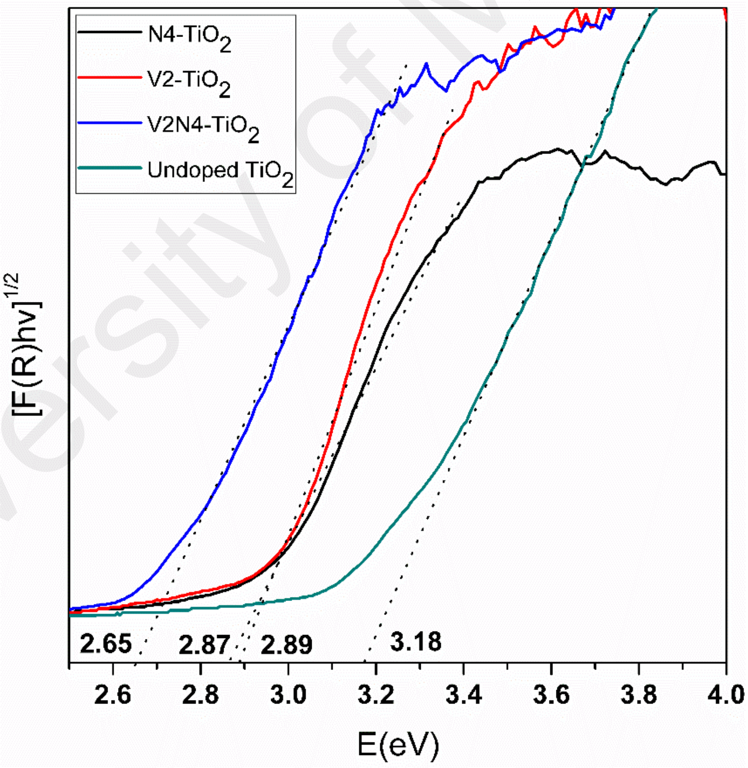

Figure 4.22: Kubelka-Munk function versus energy plots of synthesised undoped TiO_2, vanadium doped, nitrogen doped TiO_2 and vanadium nitrogen co-doped TiO_2

4.4.4 Raman Spectroscopy

Raman spectra of undoped TiO_2, vanadium doped, and nitrogen doped TiO_2 are shown in Figure 4.23. All samples show Raman peaks centred at 144, 395, 515, and 637 cm^{-1}, which are attributed to the E_g, B_{1g}, A_{1g}, and B_{2g} modes, respectively, of the anatase phase of TiO_2 (Yanagisawa & Ovenstone, 1999). This clearly indicates that the anatase crystal structure of the TiO_2 is well maintained even post-cation (V^{5+}/V^{4+}) doping. In all of the doped TiO_2, no rutile band was observed at 446 cm^{-1} (E_g), which confirms the results reported by the XRD spectrum (Phung *et al.*, 2015).

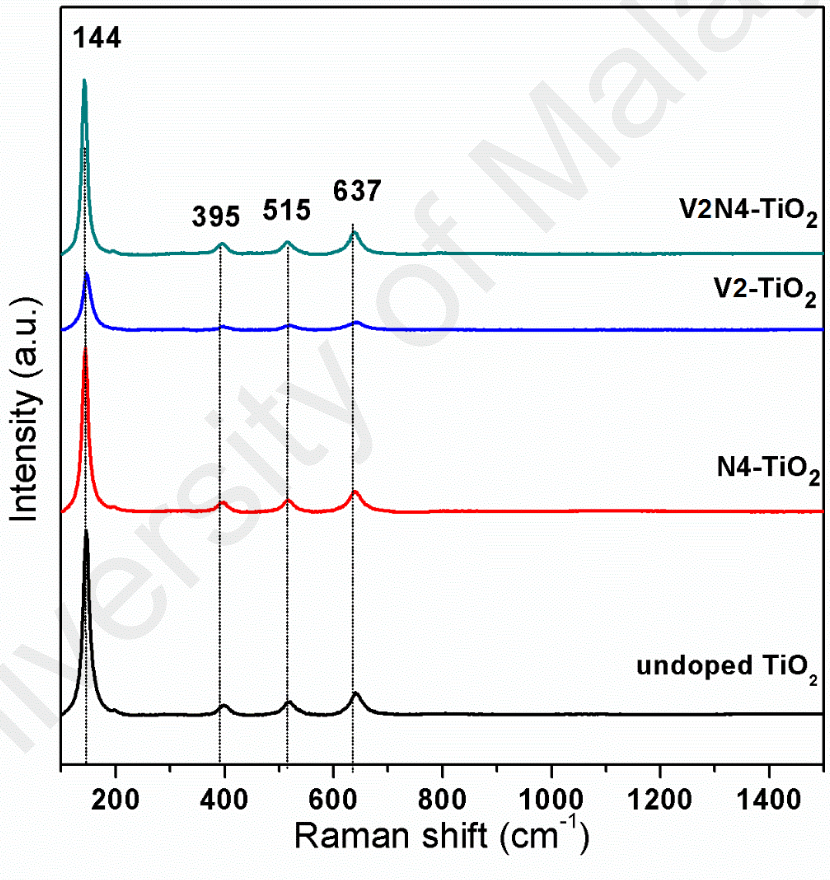

Figure 4.23: Raman spectra of synthesised undoped TiO_2, vanadium doped, nitrogen doped TiO_2 and vanadium nitrogen co-doped TiO_2

4.4.5 Field Emission Scanning Electron Microscopy (FESEM)

Figure 4.24 presents the FESEM images of undoped TiO_2, V doped TiO_2, N doped TiO_2, and VN co-doped TiO_2. The undoped TiO_2 particles showed irregular morphology due to the agglomeration of primary particles at an average diameter of ~15 nm. Increased agglomeration is more apparent in Nitrogen doped TiO_2 and VN co-doped TiO_2. The nitridation process occurs when Nitrogen doping causes the particles to agglomerate. For Vanadium doped TiO_2, the dispersion of the particles is more uniform due to its lower tendency to agglomerate.

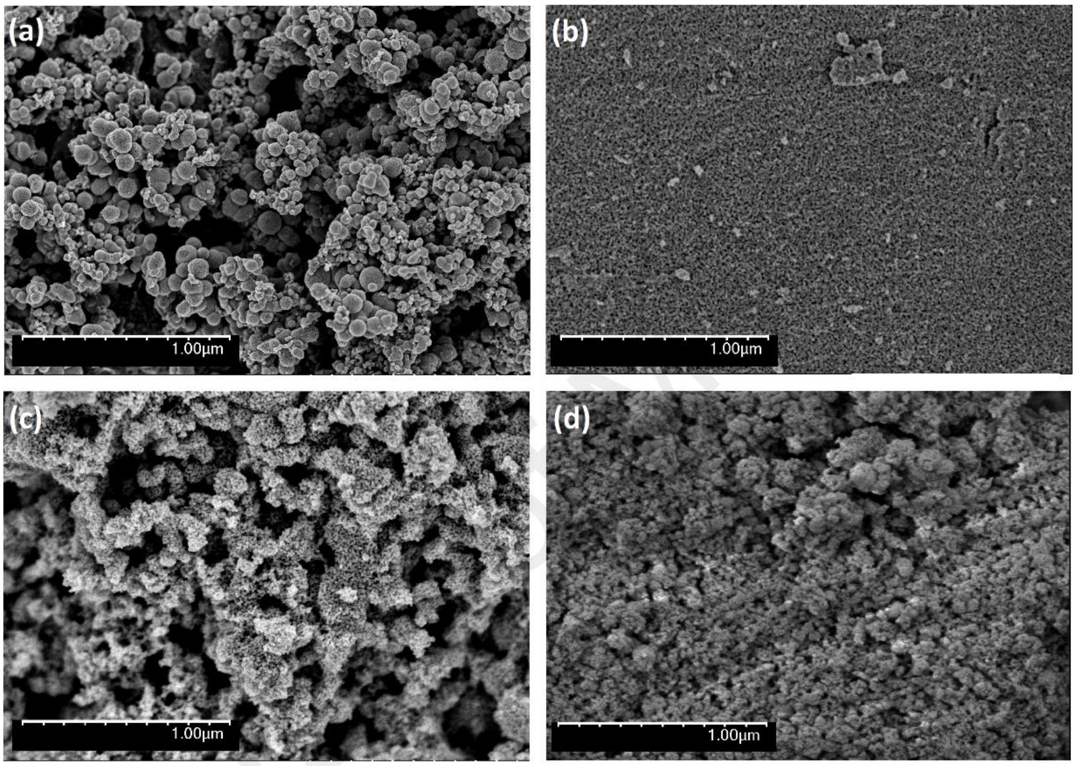

Figure 4.24: FESEM images of synthesised (a) undoped TiO_2, (b) Vanadium doped TiO_2 (V2-TiO_2) (c) Nitrogen doped TiO_2 (N4-TiO_2) and (d) Vanadium Nitrogen co-doped TiO_2 (V2N4-TiO_2)

4.4.6 Energy Dispersive X-ray (EDX)

The elemental composition for the undoped TiO_2, Vanadium doped TiO_2 and Nitrogen doped TiO_2 were determined using EDX analysis. The EDX spectra of Vanadium Nitrogen co-doped TiO_2 is shown in Figure 4.25. The highest weight percent of titanium and oxygen shows that they are the main components, at 70.42 % and 28.26 %, respectively, while for nitrogen and vanadium, it was 1.21 % and 0.11 %, respectively, which confirms the incorporation of vanadium and nitrogen within the lattice structure of TiO_2.

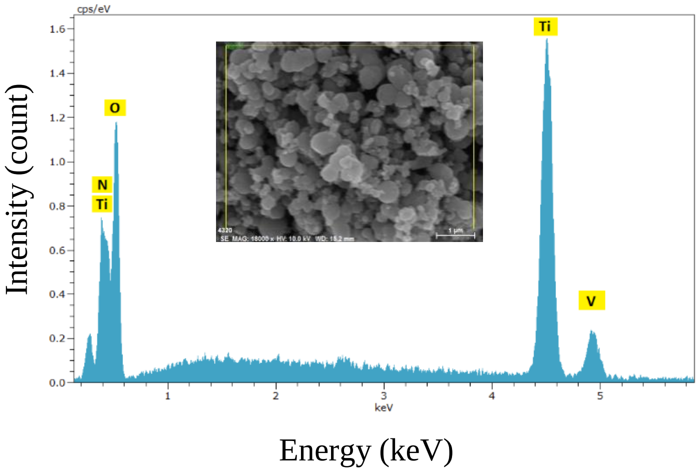

El	Series	Norm. C (wt. %)	Atom. C (at. %)
O	K-series	28.26	36.51
Ti	K-series	70.42	46.78
V	K-series	0.11	4.48
N	K-series	1.21	12.23
	Total:	100.00	100.00

Figure 4.25: EDX spectra of synthesised vanadium nitrogen co-doped TiO_2 (V2N4-TiO_2)

4.4.7 X-ray Photoelectron Spectroscopy (XPS)

The chemical states of the dopants incorporated into TiO_2 were investigated using XPS. The core level of Ti 2p, V 2p, and N 1s in V2N4 co-doped TiO_2 photocatalyst is shown in Figure 4.26. In Ti 2p XPS spectrum, two peaks, at 461.0 eV and 465.7 eV, assigned to Ti $2p_{3/2}$ and Ti $2p_{1/2}$, correspond to Ti^{4+} (Diebold, 2003). Small amounts of Ti^{3+} species at 455.3 eV was observed after the deconvolution of Ti $2p_{3/2}$ peak, which indicates oxygen vacancies created by the N doping, meaning that the vanadium and nitrogen ions are incorporated into the Ti-O lattice and influence the local chemical state of Ti^{4+} ions (JiasongZhong *et al.*, 2014).

In the V 2p XPS spectrum, two peaks at 524 eV and 519 eV are attributed to V^{5+} (Xia Yang *et al.*, 2010). Small amounts of V^{4+} at a lower binding energy (515 eV) indicates that V exists in TiO_2 in the form of V^{5+} and V^{4+}, with higher quantities of V^{5+} ions, as indicated by the area under the peak in the XPS spectrum. This suggests that V species exist in the forms of V^{4+} and V^{5+} in the V-doped TiO_2 matrix. Obviously, some V^{4+} ions were oxidized into V^{5+} in the preparation process, because vanadium existed only as V^{4+} in the precursor; the formation of V^{5+} possibly occurred during annealing (Klosek & Raftery, 2001). In addition, due to similar radii, V^{4+} ions may be incorporated in the TiO_2 lattice by replacing Ti^{4+} ions and forming Ti-O-V bonds (Wu & Chen, 2004).

In the N_{1s} XPS spectrum, a broad peak ranging from 398 - 405 eV was observed, which could be deconvoluted into two peaks at 399.8 eV and 401.6 eV. Few early reports pointed out that the N_{1s} peak at 396 eV is responsible for N ions substituting oxygen ions in the TiO_2 lattice due to the binding energy being close to the Ti-N bond (Asahi *et al.*, 2014; Asahi *et al.*, 2001). This peak is absent in our V2N4 co-doped TiO_2. However, several recent articles also reported the absence of the 396 eV peak, instead, peaks at higher binding energies at 400 eV and 402 eV were observed, which are attributed to O-Ti-N linkage and Ti-N-O linkage, respectively. This result shows that N atoms are present in both substitutional and interstitial sites in TiO_2 lattice, consequently initiating noticeable light affectability.

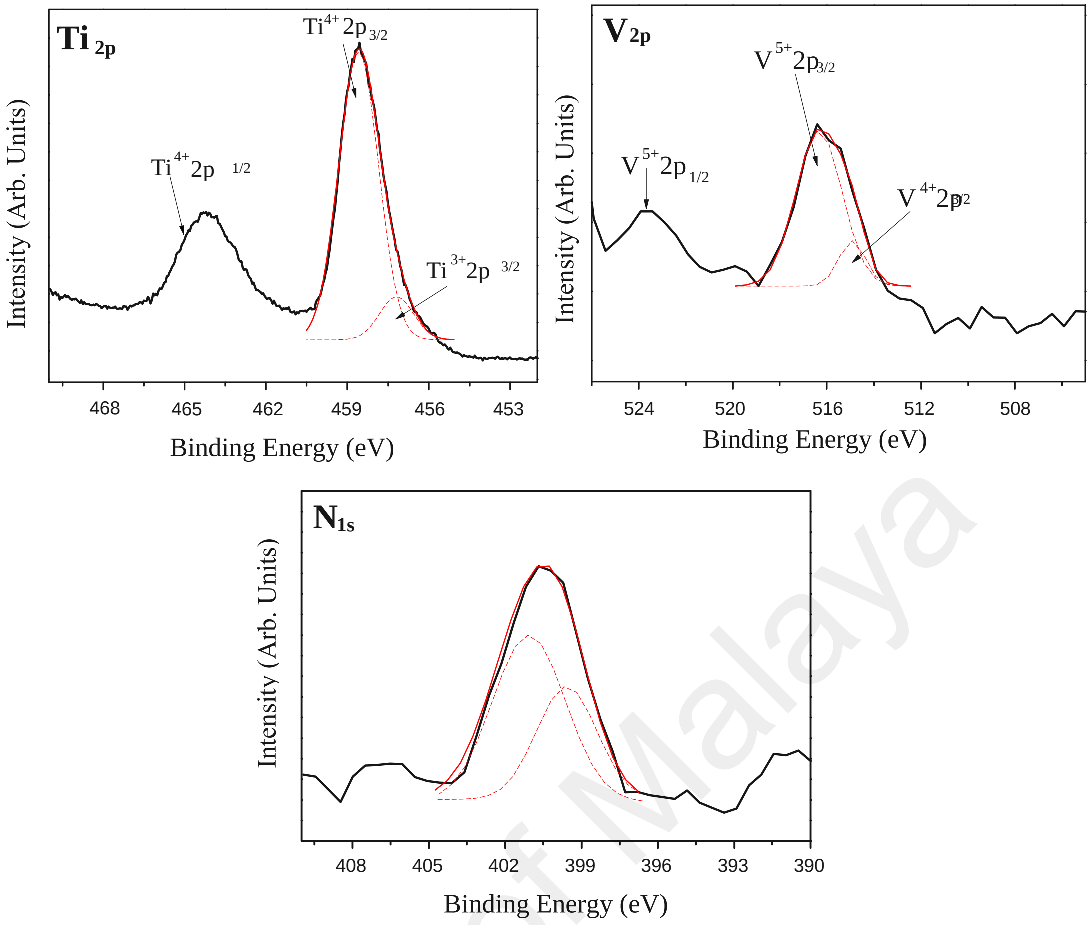

Figure 4.26: XPS Spectra of Ti 2p, V 2p and N 1s levels of V2N4 co-doped TiO_2

4.5 Photocatalytic Activity

4.5.1 Vanadium doped TiO_2 nanoparticles

The photocatalytic activity of vanadium doped TiO_2 was investigated under visible light (Figure 4.27). Amongst all vanadium doped TiO_2 photocatalysts, V2-TiO_2 was showed better performance in degradation of methylene blue. Low concentrations of vanadium demonstrated enhanced photocatalytic efficiency, both due to the increased lifetime of photogenerated charges and the extension of the absorption range (Wu & Chen, 2004). This result was supported from DRS result where in low concentration of vanadium, it gives large decreasing of band gap (Table 4.1)

Ideally, metal ions, at low concentrations, act as trapping centres for photo-generated electron (e^-) and/or hole (h^+) within the TiO_2 band gap, thus increasing the recombination time of e^-/h^+ pairs (JiasongZhong *et al.*, 2014).

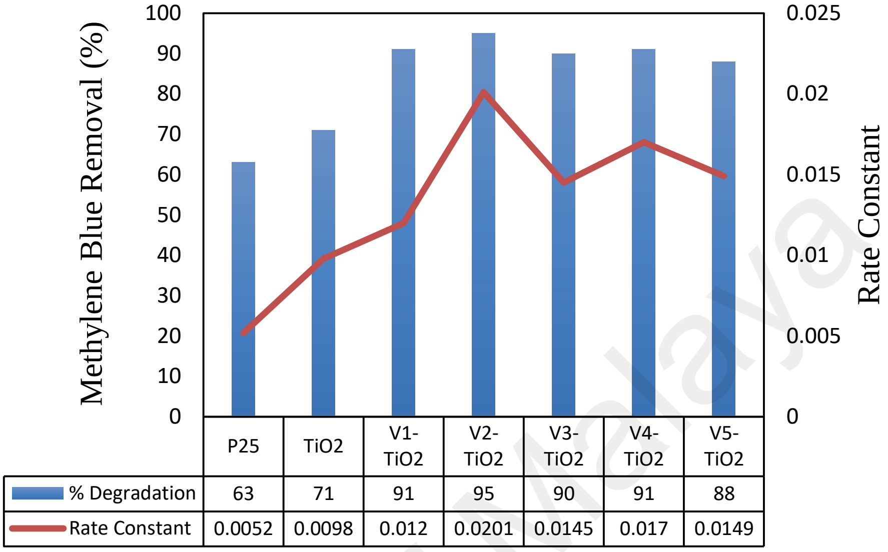

	P25	TiO2	V1-TiO2	V2-TiO2	V3-TiO2	V4-TiO2	V5-TiO2
% Degradation	63	71	91	95	90	91	88
Rate Constant	0.0052	0.0098	0.012	0.0201	0.0145	0.017	0.0149

Figure 4.27: Percentage of photocatalytic degradation of methylene blue removal among vanadium doped TiO_2 and corresponding rate constant

4.5.2 Nitrogen doped TiO_2 nanoparticles

The photocatalytic activity of nitrogen doped TiO_2 was investigated under visible light (Figure 4.28). Amongst all photocatalysts, N4-TiO_2 performed well in removing methylene blue. Additional impurity states above the valence band, coupled with oxygen vacancies in nitrogen doped TiO_2 facilitates visible light absorption, which results in more photons being absorbed onto the catalysts surface and reduced band gaps (Figures 4.14). Moreover, the improved nitrogen doped TiO_2 crystallinity helps improve charge carrier mobility (Table 4.3) (Zainal *et al.*, 2015). In higher loading of nitrogen, only the anatase phase was present, which increases the catalyst’s affinity towards oxygen molecules for the generation of superoxide radicals (Chakrabortty & Gupta, 2015). Figure 4.28 also illustrates the photocatalytic activity for all nitrogen doped TiO_2 photocatalyst under visible light using TiO_2 doped with different nitrogen loadings. It was observed that the first order of reaction constants was dependent on the amount of nitrogen loaded onto TiO_2.

However, higher nitrogen loading does not necessarily favour photocatalytic reactions due to the rapid electrons and holes recombination (Shon *et al.*, 2008). This phenomenon concluded that the necessity of slow electron/hole recombination, as well having the ability to absorb large concentrations of photons is important.

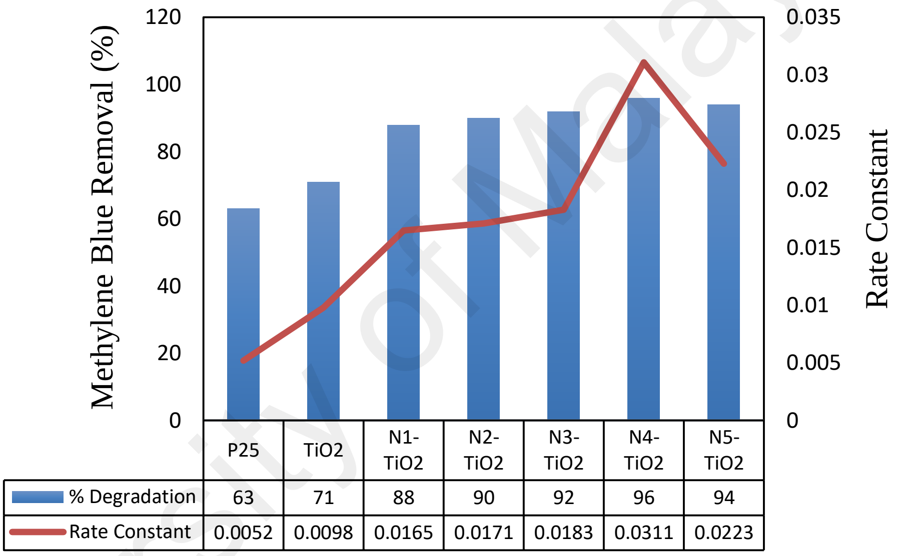

	P25	TiO2	N1-TiO2	N2-TiO2	N3-TiO2	N4-TiO2	N5-TiO2
▬ % Degradation	63	71	88	90	92	96	94
▬ Rate Constant	0.0052	0.0098	0.0165	0.0171	0.0183	0.0311	0.0223

Figure 4.28: Percentage of photocatalytic degradation of methylene blue removal among nitrogen doped TiO_2 and corresponding rate constant

4.5.3 Vanadium Nitrogen co-doped TiO_2 nanoparticles

The synergy between vanadium and nitrogen in TiO_2 (V2N4-TiO_2) was shown to tremendously improve the photocatalytic degradation of methylene blue under visible light. Figure 4.29 shows that the highest rate of photocatalytic activity was obtained by V2N4-TiO_2 with 0.0516 min^{-1} with 99 % degradation of methylene blue in 120 min. Clearly, the synergy between vanadium and nitrogen enables better photocatalytic activity improvement in the visible region.

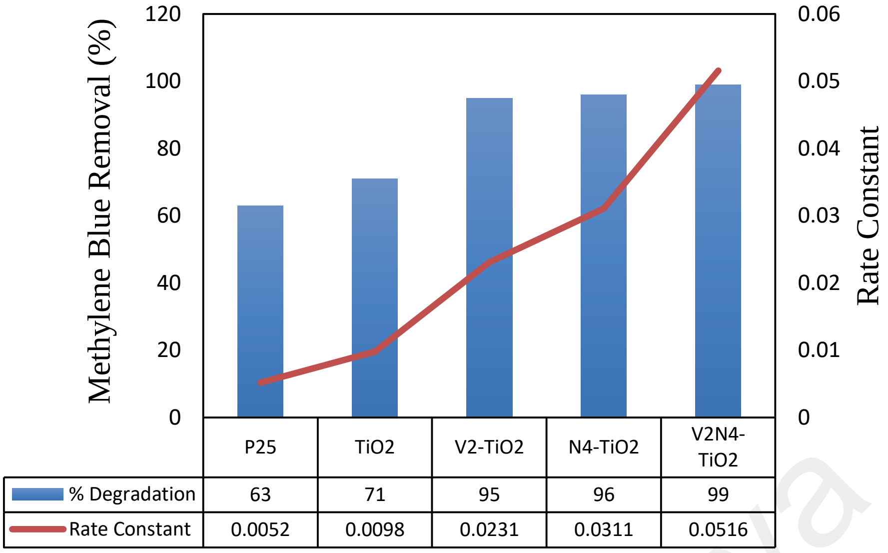

Figure 4.29: Percentage of photocatalytic degradation of methylene blue removal and corresponding rate constant

4.5.4 Comparison of all prepared photocatalyst

The sequence of photocatalytic degradation rate of methylene blue was as follows; vanadium nitrogen co-doped TiO_2 > nitrogen doped and vanadium doped TiO_2 > undoped TiO_2 > Degussa P25 (Figure 4.30).

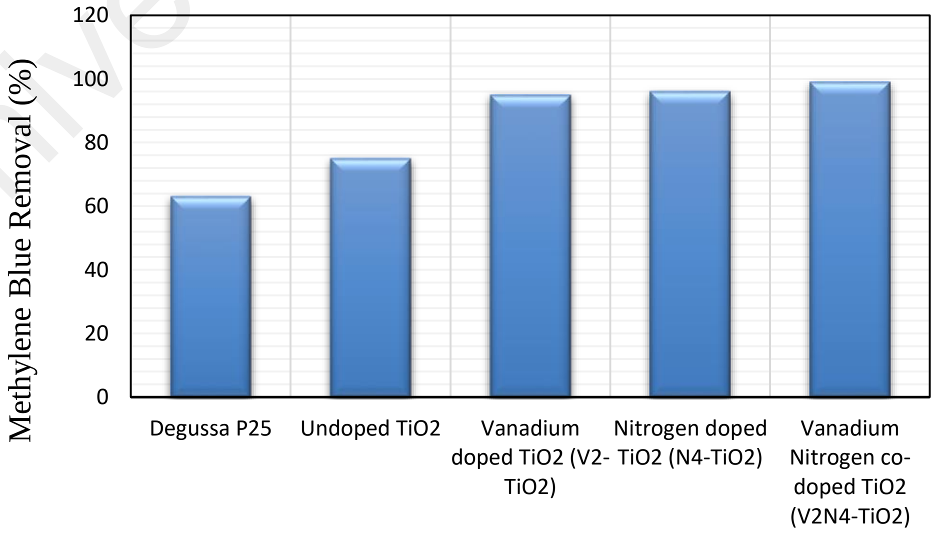

Figure 4.30: Overall photocatalytic activity for methylene blue degradation under visible light (λ at 420 to 1000 nm)

Within 120 min of photocatalytic activity, more than 95 % of 10.0 mg/l methylene blue was removed using Vanadium Nitrogen co-doped TiO_2, which meets the environmental requirement. Other than that, co-doped TiO_2 (vanadium and nitrogen) also shows the photocatalytic activity among the others with 99 % of MB degradation in 120 minutes while for the others, nitrogen doped TiO_2 (96 %), vanadium doped TiO_2 (95 %) undoped TiO_2 (75 %) and commercial Degussa P25 (63 %)

CHAPTER 5: CONCLUSION AND RECOMMENDATI ONS

5.1 Conclusion

Catalyst TiO_2, single doped TiO_2 and co-doped TiO_2 was successfully synthesised by modification of sol gel procedure, yielding fine powder. In characterisation, all catalyst includes undoped, single doped and co-doped TiO_2 were shows mesoporous pores in the range of 2 to 50 nm. Other than that, the band gaps for most of synthesised catalyst were reduced significantly especially for single doped and co-doped TiO_2.

The photocatalytic activity of vanadium nitrogen co-doped TiO_2 (V2N4-TiO_2) shows highest percent of degradation of methylene blue with 99 % among the rest of catalyst. The photocatalytic activity of vanadium and nitrogen single doped TiO_2 was studied to determine the optimum weight percent for each element. Based on these results, the optimum weight percent for vanadium (0.125 %) and nitrogen (0.750 %) were selected to study methylene blue degradation with vanadium nitrogen co-doped TiO_2.

The increased photocatalytic activity of the co-doped TiO_2 samples can be associate to the synergistic effects caused by vanadium and nitrogen, which increases the visible light absorption while simultaneously acting as electron and hole trapping sites, which decreases the rate of charge recombination by forming a new energy level for TiO_2.

5.2 Recommendations for future work

A few strategies could be employed to increase the efficiency of photocatalytic activity of TiO_2. The structures and properties of TiO_2 could be modified via new approaches, such as introducing hydrogenation reactions after synthesising TiO_2. This technique is compatible with various method of synthesising powdered-TiO_2, such as sol-gel, hydrothermal, and solvothermal methods. Hydrogenated vanadium nitrogen co-doped TiO_2 can improve photocatalytic activity due to the formation of surface disorder, which acts as active sites and enhances the mobility of the electrons.

Since vanadium nitrogen co-doped TiO_2 is a highly active photocatalyst, it can be used as thin films or membranes. Handling thin films is much easier compared to TiO_2 powder in the context of separation and recovery. Thin film with thicknesses of less than 100 nm can be obtained from the spin coating technique, where the prepared TiO_2 powder is mixed with a suitable film forming solvent prior to the spinning process. Another alternative approach is to prepare vanadium nitrogen co-doped TiO_2 as sol-gel precursors, followed by spin or dip coating on a substrate prior to annealing it.

REFERENCES

Agarwala, S., & Ho, G. (2009). Synthesis and tuning of ordering and crystallinity of mesoporous titanium dioxide film. *Materials Letters, 63*(18), 1624-1627.

Ahmed, S., Rasul, M., Martens, W. N., Brown, R., & Hashib, M. (2010). Heterogeneous photocatalytic degradation of phenols in wastewater: a review on current status and developments. *Desalination, 261*(1), 3-18.

Ahmed, S., Rasul, M. G., Martens, W. N., Brown, R., & Hashib, M. A. (2010). Heterogeneous photocatalytic degradation of phenols in wastewater: A review on current status and developments. *Desalination, 261*(1–2), 3-18.

Akpan, U., & Hameed, B. (2009). Parameters affecting the photocatalytic degradation of dyes using TiO_2 -based photocatalysts: a review. *Journal of hazardous materials, 170*(2), 520-529.

Akpan, U., & Hameed, B. (2010). The advancements in sol–gel method of doped-TiO_2 photocatalysts. *Applied Catalysis A: General, 375*(1), 1-11.

Alfano, O. M., Cabrera, M. a. I., & Cassano, A. E. (1997). Photocatalytic reactions involving hydroxyl radical attack. *Journal of Catalysis, 172*(2), 370-379.

Allegre, C., Moulin, P., Maisseu, M., & Charbit, F. (2006). Treatment and reuse of reactive dyeing effluents. *Journal of Membrane Science, 269*(1), 15-34.

Ananpattarachai, J., Kajitvichyanukul, P., & Seraphin, S. (2009). Visible light absorption ability and photocatalytic oxidation activity of various interstitial N-doped TiO_2 prepared from different nitrogen dopants. *Journal of hazardous materials, 168*(1), 253-261.

Antonelli, D. M., & Ying, J. Y. (1995). Synthesis of hexagonally packed mesoporous TiO_2 by a modified sol–gel method. *Angewandte Chemie International Edition in English, 34*(18), 2014-2017.

Asahi, R., Morikawa, T., Irie, H., & Ohwaki, T. (2014). Nitrogen-doped titanium dioxide as visible-light-sensitive photocatalyst: designs, developments, and prospects. *Chemical reviews, 114*(19), 9824-9852.

Asahi, R., Morikawa, T., Ohwaki, T., Aoki, K., & Taga, Y. (2001). Visible-light photocatalysis in nitrogen-doped titanium oxides. *science, 293*(5528), 269-271.

Avansi, W., Arenal, R., de Mendonca, V., Ribeiro, C., & Longo, E. (2014). Vanadium-doped TiO_2 anatase nanostructures: the role of V in solid solution formation and its effect on the optical properties. *CrystEngComm, 16*(23), 5021-5027.

Bach, U., Lupo, D., Comte, P., Moser, J., Weissörtel, F., Salbeck, J., Grätzel, M. (1998). Solid-state dye-sensitized mesoporous TiO_2 solar cells with high photon-to-electron conversion efficiencies. *Nature, 395*(6702), 583-585.

Balachandran, U., & Eror, N. (1982). Raman spectra of titanium dioxide. *Journal of Solid State Chemistry, 42*(3), 276-282.

Balasubramanian, G., Dionysiou, D. D., Suidan, M. T., Baudin, I., & Laıné, J.-M. (2004). Evaluating the activities of immobilized TiO_2 powder films for the photocatalytic degradation of organic contaminants in water. *Applied Catalysis B: Environmental, 47*(2), 73-84.

Bañares, M. A., Alemany, L. s. J., Jiménez, M. C., Larrubia, M. A., Delgado, F., Granados, M. L., . . . Fierro, J. L. s. G. (1996). The role of vanadium oxide on the titania transformation under thermal treatments and surface vanadium states. *Journal of Solid State Chemistry, 124*(1), 69-76.

Bhatkhande, D. S., Pangarkar, V. G., & Beenackers, A. A. (2002). Photocatalytic degradation for environmental applications–a review. *Journal of Chemical Technology and Biotechnology, 77*(1), 102-116.

Carp, O., Huisman, C. L., & Reller, A. (2004). Photoinduced reactivity of titanium dioxide. *Progress in solid state chemistry, 32*(1), 33-177.

Castellote, M., & Bengtsson, N. (2011). Principles of TiO_2 Photocatalysis *Applications of Titanium Dioxide Photocatalysis to Construction Materials* (pp. 5-10): Springer.

Chakrabarti, S., & Dutta, B. K. (2004). Photocatalytic degradation of model textile dyes in wastewater using ZnO as semiconductor catalyst. *Journal of hazardous materials, 112*(3), 269-278.

Chakrabortty, D., & Gupta, S. S. (2015). Removal of Orange II dye from aqueous solution by adsorption and photodegradation with visible light in presence of nitrogen doped titania nanocatalyst. *Indian Journal of Chemical Technology, 22*(1-2), 34-41.

Chen, X., Li, C., Grätzel, M., Kostecki, R., & Mao, S. S. (2012). Nanomaterials for renewable energy production and storage. *Chemical Society Reviews, 41*(23), 7909-7937.

Chen, X., & Mao, S. S. (2007). Titanium dioxide nanomaterials: synthesis, properties, modifications, and applications. *Chem. Rev, 107*(7), 2891-2959.

Cheng, X., Yu, X., Xing, Z., & Wan, J. (2012). Enhanced photocatalytic activity of nitrogen doped TiO_2 anatase nano-particle under simulated sunlight irradiation. *Energy Procedia, 16*, 598-605.

Chhowalla, M., Shin, H. S., Eda, G., Li, L.-J., Loh, K. P., & Zhang, H. (2013). The chemistry of two-dimensional layered transition metal dichalcogenide nanosheets. *Nature chemistry, 5*(4), 263-275.

Choi, W., Termin, A., & Hoffmann, M. R. (1994). The role of metal ion dopants in quantum-sized TiO_2: correlation between photoreactivity and charge carrier recombination dynamics. *The Journal of Physical Chemistry, 98*(51), 13669-13679.

Clark, R. M., Rossman, L. A., & Wymer, L. J. (1995). Modeling distribution system water quality: Regulatory implications. *Journal of water resources planning and management, 121*(6), 423-428.

Collazzo, G. C., Foletto, E. L., Jahn, S. L., & Villetti, M. A. (2012). Degradation of Direct Black 38 dye under visible light and sunlight irradiation by N-doped anatase TiO_2 as photocatalyst. *Journal of environmental management, 98*, 107-111.

Colmenares, J. C., Luque, R., Campelo, J. M., Colmenares, F., Karpiński, Z., & Romero, A. A. (2009). Nanostructured photocatalysts and their applications in the photocatalytic transformation of lignocellulosic biomass: an overview. *Materials, 2*(4), 2228-2258.

Dąbrowski, A. (2001). Adsorption—from theory to practice. *Advances in colloid and interface science, 93*(1), 135-224.

Darzi, S. J., Mahjoub, A., & Sarfi, S. (2012). Visible-light-active nitrogen doped TiO_2 nanoparticles prepared by sol–gel acid catalyzed reaction. *Iran. J. Mater. Sci. Eng, 9*(3), 17-23.

Deng, Y., Wei, J., Sun, Z., & Zhao, D. (2013). Large-pore ordered mesoporous materials templated from non-Pluronic amphiphilic block copolymers. *Chemical Society Reviews, 42*(9), 4054-4070.

Di Valentin, C., Pacchioni, G., Selloni, A., Livraghi, S., & Giamello, E. (2005). Characterization of paramagnetic species in N-doped TiO_2 powders by EPR spectroscopy and DFT calculations. *The Journal of Physical Chemistry B, 109*(23), 11414-11419.

Diebold, U. (2003). Structure and properties of TiO_2 surfaces: a brief review. *Applied physics A, 76*(5), 681-687.

Ding, X.-Z., Liu, X.-H., & He, Y.-Z. (1996). Grain size dependence of anatase-to-rutile structural transformation in gel-derived nanocrystalline titania powders. *Journal of materials science letters, 15*(20), 1789-1791.

Djurisic, A. B., Leung, Y. H., & Ching Ng, A. M. (2014). Strategies for improving the efficiency of semiconductor metal oxide photocatalysis. *Materials Horizons, 1*(4), 400-410. doi:10.1039/C4MH00031E

Doong, R.-a., Chang, P.-Y., & Huang, C.-H. (2009). Microstructural and photocatalytic properties of sol–gel-derived vanadium-doped mesoporous titanium dioxide nanoparticles. *Journal of Non-Crystalline Solids, 355*(45), 2302-2308.

Du Pasquier, A., Stewart, M., Spitler, T., & Coleman, M. (2009). Aqueous coating of efficient flexible TiO 2 dye solar cell photoanodes. *Solar Energy Materials and Solar Cells, 93*(4), 528-535.

Eswar, N. K., Ramamurthy, P. C., & Madras, G. (2016). Novel synergistic photocatalytic degradation of antibiotics and bacteria using V–N doped TiO_2 under visible light: the state of nitrogen in V-doped TiO_2. *New Journal of Chemistry, 40*(4), 3464-3475.

Fujishima, A., Rao, T. N., & Tryk, D. A. (2000). Titanium dioxide photocatalysis. *Journal of Photochemistry and Photobiology C: Photochemistry Reviews, 1*(1), 1-21.

Gaya, U. I. (2014). Principles of Heterogeneous Photocatalysis *Heterogeneous Photocatalysis Using Inorganic Semiconductor Solids* (pp. 1-41): Springer.

Geetha, K., & Velmani, N. (2015). Diverse Technology and Methods for Dye Treatment. *Asian Journal of Chemistry, 27*(4), 1177.

Giles, C. H., Smith, D., & Huitson, A. (1974). A general treatment and classification of the solute adsorption isotherm. I. Theoretical. *Journal of Colloid and Interface Science, 47*(3), 755-765.

Grätzel, M. (2001). Photoelectrochemical cells. *Nature, 414*(6861), 338-344.

Guettai, N., & Amar, H. A. (2005). Photocatalytic oxidation of methyl orange in presence of titanium dioxide in aqueous suspension. Part II: kinetics study. *Desalination, 185*(1), 439-448.

Gupta, S. M., & Tripathi, M. (2011). A review of TiO_2 nanoparticles. *Chinese Science Bulletin, 56*(16), 1639-1657.

Harris, J., & McCartor, A. (2011). The World'S Worst Toxic Pollution Problems Report 2011. *Blacksmith Institute*, 1-76.

He, Z., Que, W., Chen, J., Yin, X., He, Y., & Ren, J. (2012). Photocatalytic degradation of methyl orange over nitrogen–fluorine codoped TiO_2 nanobelts prepared by solvothermal synthesis. *ACS applied materials & interfaces, 4*(12), 6816-6826.

Irie, H., Washizuka, S., & Hashimoto, K. (2006). Hydrophilicity on carbon-doped TiO_2 thin films under visible light. *Thin Solid Films, 510*(1), 21-25.

Jaiswal, R., Patel, N., Kothari, D., & Miotello, A. (2012). Improved visible light photocatalytic activity of TiO_2 co-doped with Vanadium and Nitrogen. *Applied Catalysis B: Environmental, 126*, 47-54.

JiasongZhong, Xu, J., & Wang, Q. (2014). Nitrogen and vanadium Co-doped TiO_2 mesosponge layers for enhancement in visible photocatalytic activity. *Applied Surface Science, 315*, 131-137.

Khan, H., & Berk, D. (2013). Sol–gel synthesized vanadium doped TiO_2 photocatalyst: physicochemical properties and visible light photocatalytic studies. *Journal of sol-gel science and technology, 68*(2), 180-192.

Khan, M., Gul, S. R., Li, J., Cao, W., & Mamalis, A. G. (2015). Preparation, characterization and visible light photocatalytic activity of silver, nitrogen co-doped TiO_2 photocatalyst. *Materials Research Express, 2*(6), 066201.

Kitano, M., Mitsui, R., Eddy, D. R., El-Bahy, Z. M., Matsuoka, M., Ueshima, M., & Anpo, M. (2007). Synthesis of nanowire TiO_2 thin films by hydrothermal treatment and their photoelectrochemical properties. *Catalysis Letters, 119*(3-4), 217-221.

Klosek, S., & Raftery, D. (2001). Visible light driven V-doped TiO_2 photocatalyst and its photooxidation of ethanol. *The Journal of Physical Chemistry B, 105*(14), 2815-2819.

Kortüm, G., Braun, W., & Herzog, G. (1963). Principles and Techniques of Diffuse-Reflectance Spectroscopy. *Angewandte Chemie International Edition in English, 2*(7), 333-341.

Koswojo, R., Utomo, R. P., Ju, Y.-H., Ayucitra, A., Soetaredjo, F. E., Sunarso, J., & Ismadji, S. (2010). Acid Green 25 removal from wastewater by organo-bentonite from Pacitan. *Applied clay science, 48*(1), 81-86.

Lin, W.-C., & Lin, Y.-J. (2012). Effect of vanadium (IV)-doping on the visible light-induced catalytic activity of titanium dioxide catalysts for methylene blue degradation. *Environmental engineering science, 29*(6), 447-452.

Linsebigler, A. L., Lu, G., & Yates Jr, J. T. (1995). Photocatalysis on TiO_2 surfaces: principles, mechanisms, and selected results. *Chemical reviews, 95*(3), 735-758.

Liu, C., Tang, X., Mo, C., & Qiang, Z. (2008). Characterization and activity of visible-light-driven TiO 2 photocatalyst codoped with nitrogen and cerium. *Journal of Solid State Chemistry, 181*(4), 913-919.

Liu, Y., Chen, X., Li, J., & Burda, C. (2005). Photocatalytic degradation of azo dyes by nitrogen-doped TiO 2 nanocatalysts. *Chemosphere, 61*(1), 11-18.

Lucky, R. A., Sui, R., Lo, J. M., & Charpentier, P. A. (2010). Effect of Solvent on the Crystal Growth of One-Dimensional ZrO2− TiO_2 Nanostructures. *Crystal Growth & Design, 10*(4), 1598-1604.

Luo, H., Wang, C., & Yan, Y. (2003). Synthesis of mesostructured titania with controlled crystalline framework. *Chemistry of materials, 15*(20), 3841-3846.

Mahshid, S., Askari, M., & Ghamsari, M. S. (2007). Synthesis of TiO_2 nanoparticles by hydrolysis and peptization of titanium isopropoxide solution. *Journal of Materials Processing Technology, 189*(1), 296-300.

Malekshahi Byranvand, M., Nemati Kharat, A., Fatholahi, L., & Malekshahi Beiranvand, Z. (2013). A review on synthesis of nano-TiO_2 via different methods. *Journal of nanostructures, 3*(1), 1-9.

McMullan, G., Meehan, C., Conneely, A., Kirby, N., Robinson, T., Nigam, P., . . . Smyth, W. (2001). Microbial decolourisation and degradation of textile dyes. *Applied Microbiology and Biotechnology, 56*(1), 81-87.

Neppolian, B., Choi, H., Sakthivel, S., Arabindoo, B., & Murugesan, V. (2002). Solar light induced and TiO_2 assisted degradation of textile dye reactive blue 4. *Chemosphere, 46*(8), 1173-1181.

Padmanabhan, S. C., Pillai, S. C., Colreavy, J., Balakrishnan, S., McCormack, D. E., Perova, T. S., . . . Kelly, J. M. (2007). A simple sol− gel processing for the development of high-temperature stable photoactive anatase titania. *Chemistry of materials, 19*(18), 4474-4481.

Park, H., Park, Y., Kim, W., & Choi, W. (2013). Surface modification of TiO_2 photocatalyst for environmental applications. *Journal of Photochemistry and Photobiology C: Photochemistry Reviews, 15*, 1-20.

Park, J.-Y., Lee, C., Jung, K.-W., & Jung, D. (2009). Structure related photocatalytic properties of TiO_2. *Bull. Korean Chem. Soc, 30*(2), 402-404.

Patterson, A. (1939). The Scherrer formula for X-ray particle size determination. *Physical review, 56*(10), 978.

Peng, T., Zhao, D., Dai, K., Shi, W., & Hirao, K. (2005). Synthesis of titanium dioxide nanoparticles with mesoporous anatase wall and high photocatalytic activity. *The Journal of Physical Chemistry B, 109*(11), 4947-4952.

Pookmanee, P., & Phanichphant, S. (2009). Titanium dioxide powder prepared by a sol-gel method. *Journal of Ceramic Processing Research, 10*(2), 167-170.

Rosborg, I., Nihlgård, B., Gerhardsson, L., & Sverdrup, H. (2006). Concentrations of inorganic elements in 20 municipal waters in Sweden before and after treatment–links to human health. *Environmental geochemistry and health, 28*(3), 215-229.

Samsudin, E. M., Hamid, S. B. A., Juan, J. C., Basirun, W. J., & Centi, G. (2015). Enhancement of the intrinsic photocatalytic activity of TiO_2 in the degradation of 1, 3, 5-triazine herbicides by doping with N, F. *Chemical Engineering Journal, 280*, 330-343.

Samsudin, E. M., Hamid, S. B. A., Juan, J. C., Basirun, W. J., Kandjani, A. E., & Bhargava, S. K. (2015). Controlled nitrogen insertion in titanium dioxide for optimal photocatalytic degradation of atrazine. *RSC Advances, 5*(55), 44041-44052.

Santana-Aranda, M., Morán-Pineda, M., Hernández, J., & Castillo, S. (2005). Physical Properties of TiO_2 Prepared by Sol-Gel Under Different pH Conditions for Photocatalysis. *Superficies y Vacío, 18*(1), 46-49.

Sathish, M., Viswanathan, B., Viswanath, R., & Gopinath, C. S. (2005). Synthesis, characterization, electronic structure, and photocatalytic activity of nitrogen-doped TiO_2 nanocatalyst. *Chemistry of materials, 17*(25), 6349-6353.

Schneider, J., Matsuoka, M., Takeuchi, M., Zhang, J., Horiuchi, Y., Anpo, M., & Bahnemann, D. W. (2014). Understanding TiO_2 photocatalysis: mechanisms and materials. *Chemical reviews, 114*(19), 9919-9986.

Shahini, S., Askari, M., & Sadrnezhaad, S. (2011). Gel–sol synthesis and aging effect on highly crystalline anatase nanopowder. *Bulletin of Materials Science, 34*(6), 1189-1195.

Shao, G. N., Imran, S., Jeon, S. J., Kang, S. J., Haider, S., & Kim, H. T. (2015). Sol–gel synthesis of vanadium doped titania: Effect of the synthetic routes and investigation of their photocatalytic properties in the presence of natural sunlight. *Applied Surface Science, 351,* 1213-1223.

Simonsen, M. E., & Søgaard, E. G. (2010). Sol–gel reactions of titanium alkoxides and water: influence of pH and alkoxy group on cluster formation and properties of the resulting products. *Journal of sol-gel science and technology, 53*(3), 485-497.

Sing, K. (2001). The use of nitrogen adsorption for the characterisation of porous materials. *Colloids and Surfaces A: Physicochemical and Engineering Aspects, 187,* 3-9.

Sing, K. S. (1985). Reporting physisorption data for gas/solid systems with special reference to the determination of surface area and porosity (Recommendations 1984). *Pure and applied chemistry, 57*(4), 603-619.

Spurr, R. A., & Myers, H. (1957). Quantitative analysis of anatase-rutile mixtures with an X-ray diffractometer. *Analytical Chemistry, 29*(5), 760-762.

Su, C., Hong, B.-Y., & Tseng, C.-M. (2004). Sol–gel preparation and photocatalysis of titanium dioxide. *Catalysis Today, 96*(3), 119-126.

Tarver, T. (2008). “Just Add Water”: Regulating and Protecting the Most Common Ingredient. *Journal of food science, 73*(1), R1-R13.

Theivasanthi, T., & Alagar, M. (2013). Titanium dioxide (TiO_2) Nanoparticles XRD Analyses: An Insight. *arXiv preprint arXiv:1307.1091*.

Thuy, N. M., Van, D. Q., & Hai, L. T. H. (2012). The Visible Light Activity of the TiO_2 and TiO_2: V^{4+} Photocatalyst. *Nanomaterials and Nanotechnology, 2*(Godište 2012), 2-14.

Wang, H.-E., Zheng, L.-X., Liu, C.-P., Liu, Y.-K., Luan, C.-Y., Cheng, H., Bello, I. (2011). Rapid microwave synthesis of porous TiO_2 spheres and their applications in dye-sensitized solar cells. *The Journal of Physical Chemistry C, 115*(21), 10419-10425.

Wang, Y., He, Y., Lai, Q., & Fan, M. (2014). Review of the progress in preparing nano TiO_2: An important environmental engineering material. *Journal of Environmental Sciences, 26*(11), 2139-2177.

Warwick, M. E., Dunnill, C. W., Goodall, J., Darr, J. A., & Binions, R. (2011). Hybrid chemical vapour and nanoceramic aerosol assisted deposition for multifunctional nanocomposite thin films. *Thin Solid Films, 519*(18), 5942-5948.

Wu, J. C.-S., & Chen, C.-H. (2004). A visible-light response vanadium-doped titania nanocatalyst by sol–gel method. *Journal of Photochemistry and Photobiology A: Chemistry, 163*(3), 509-515.

Xiang, Q., Yu, J., Wang, W., & Jaroniec, M. (2011). Nitrogen self-doped nanosized TiO_2 sheets with exposed {001} facets for enhanced visible-light photocatalytic activity. *Chemical Communications, 47*(24), 6906-6908.

Yanagisawa, K., & Ovenstone, J. (1999). Crystallization of anatase from amorphous titania using the hydrothermal technique: effects of starting material and temperature. *The Journal of Physical Chemistry B, 103*(37), 7781-7787.

Yang, X., Cao, C., Erickson, L., Hohn, K., Maghirang, R., & Klabunde, K. (2009). Photo-catalytic degradation of Rhodamine B on C-, S-, N-, and Fe-doped TiO_T under visible-light irradiation. *Applied Catalysis B: Environmental, 91*(3), 657-662.

Yang, X., Ma, F., Li, K., Guo, Y., Hu, J., Li, W. Guo, Y. (2010). Mixed phase titania nanocomposite codoped with metallic silver and vanadium oxide: new efficient photocatalyst for dye degradation. *Journal of hazardous materials, 175*(1), 429-438.

Yao, Y., Xu, F., Chen, M., Xu, Z., & Zhu, Z. (2010). Adsorption behavior of methylene blue on carbon nanotubes. *Bioresource technology, 101*(9), 3040-3046.

Zainal, N. D., Nur, H., & Ling, L. S. (2015). Synthesis and characterization of nitrogen-doped titania nanomaterials of homogeneous particle size. *Malaysian Journal of Fundamental and Applied Sciences, 11*(3).

Zaleska, A. (2008). Doped-TiO2: a review. *Recent Patents on Engineering, 2*(3), 157-164.

Zhou, J., Zhang, Y., Zhao, X., & Ray, A. K. (2006). Photodegradation of benzoic acid over metal-doped TiO_2. *Industrial & Engineering Chemistry Research, 45*(10), 3503-3511.

Zhou, W., Liu, Q., Zhu, Z., & Zhang, J. (2010). Preparation and properties of vanadium-doped TiO_2 photocatalysts. *Journal of Physics D: Applied Physics, 43*(3), 035301.

LIST OF PUBLICATIONS AND PAPERS PRESENTED

Technical paper:

Vanadium doped TiO_2 photocatalyst for visible light driven degradation of organic pollutants, Aizat Azhari Mohd Yatim, Samira Bagheri, Putla Sudarsanam, and Suresh K. Bhargava. Article reference: NANO-113404 submitted to IOP Publishing

Conference:

Influence of pH for the synthesis of nanocrystalline TiO_2 by sol-gel technique. Aizat Azhari Mohd Yatim, Emy Marlina Samsudin and Sharifah Bee Abd Hamid. Proceedings of 4th International Science Postgraduate Conference 2016 (ISPC2016) © Faculty of Science, Universiti Teknologi Malaysia

APPENDIX

Appendix A: Calibration curve of Methylene blue using UV-Vis (MB) analysis